COPERNICUS SPACE COMPONENT SENTINEL OPTICAL IMAGING

MISSION PERFORMANCE CLUSTER SERVICE

# Data Quality Report

# Sentinel-3 SLSTR - November 2023

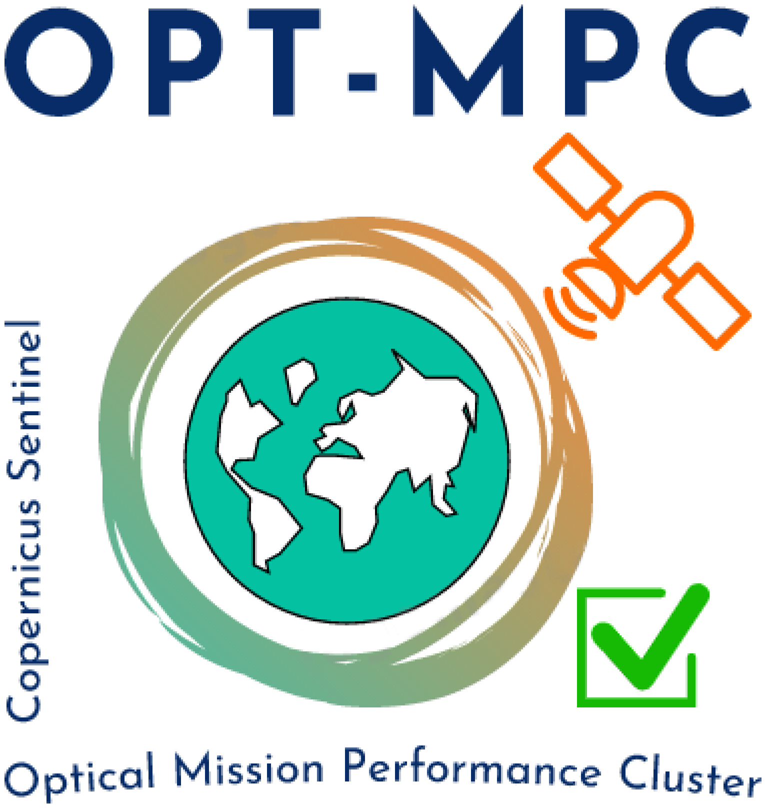

Ref.: OMPC.LDO.DQR.04.11-2023
Issue: 1.1
Date: 14/12/2023
Contract: 4000136252/21/I-BG

| | | | |
|---|---|---|---|
| **Customer:** | ESA | **Document Ref.:** | OMPC.LDO.DQR.04.11 -2023 |
| **Contract No.:** | 4000136252/21/I-BG | **Date:** | 14/12/2023 |
| | | **Issue:** | 1.1 |

| | | | |
|---|---|---|---|
| **Project:** | COPERNICUS SPACE COMPONENT SENTINEL OPTICAL IMAGING MISSION PERFORMANCE CLUSTER SERVICE | | |
| **Title:** | Data Quality Report - SLSTR - November 2023 | | |
| **Author(s):** | SLSTR ESL team | | |
| **Approved by:** | P. Paolino, OPT-MPC SLSTR ESL Coordinator | **Authorized by** | C. Henocq, OPT-MPC S3 Technical Manager |
| **Distribution:** | ESA, EUMETSAT, published in Sentinel Online | | |
| **Accepted by ESA** | S. Dransfeld, ESA TO | | |
| **Filename** | OMPC.LDO.DQR.04.11-2023 - i1r1 - SLSTR Data Quality Report November 2023.docx | | |

# Changes Log

| Version | Date | Changes |
|---|---|---|
| 1.0 | 11/12/2023 | First version |
| 1.1 | 14/12/2023 | Sections 6.2 and 6.3 removed as outdated – updates will be included shortly. |

# Table of content

# List of Figures

# List of Tables

# 1 Executive Summary

**This section provides a summary of the data quality for SLSTR-A and SLSTR-B over the month of operation.**

**Any relevant formal instrument data requirements are added under the subsequent section headers for reference.**

Each month the data measured by SLSTR-A and SLSTR-B are checked for quality and it is determined whether they meet the requirements specified in Sentinel-3 Mission Requirements Document, using the methods in the Sentinel-3 Cal-Val Plan.

A summary of the status from each check performed is provided below. A traffic light system is used, where the categories are determined as follows

- Gray indicates no change over the reporting period
- Green indicates that aspect is performing optimally
- Amber indicates there are some issues noted that may affect data quality or availability this month, or a user correction that needs to be applied
- Red indicates a significant quality issue, or instrument anomaly for some of the month

Follow the link on each topic header for more detailed information contained in this document.

| Topic | Instrument | Comments |
|---|---|---|
| Processing Baseline Version | ⬜ S3A | |
| | ⬜ S3B | |
| Event | 🟧 S3A | Several events occurred this month without impact on data quality |
| | 🟧 S3B | Several events occurred this month without impact on data quality |
| Instrument status | 🟩 S3A | |
| | 🟩 S3B | |
| Level-1 TIR Radiometric Validation | ⬜ S3A | |
| | ⬜ S3B | |
| Level- 1 VIS SWIR Radiometric Validation | 🟧 S3A | Vicarious validation indicates calibration offsets need to be applied to the VIS/SWIR channels<br>New validation results using PICS method |
| | 🟧 S3B | Vicarious validation indicates calibration offsets need to be applied to the VIS/SWIR channels<br>New validation results using PICS method |
| Level-1 Geometric Validation | 🟩 S3A | |
| | 🟩 S3B | |
| Level 2 LST validation | ⬜ S3A | |

| Topic | Instrument | Comments |
|---|---|---|
| | S3B | |
| Level 2 FRP validation | S3A | |
| | S3B | |

# 2 Processing status

## 2.1 Processing baseline status

**The Processing Baseline Version allows traceability of any changes to the software used to process the SLSTR products, and any updates to the auxiliary data files used to generate them.**

The processing baseline identifier is now provided in the manifest file and in the global attributes of each file. The identifier comprises of seven characters (e.g. SL__L1_) which indicates the product type, and seven characters to indicate its version, xxx.yy.zz (e.g. 004.04.00). The version number, xxx indicates baseline collection, yy indicates change due to the IPF or ADF and zz indicates change in system components (e.g. L0, PUG) that do not impact data quality but are included to allow full traceability.

There has been no delivery or deployment concerning SLSTR during this period. The deployed processing baseline and IPF versions are consistent with the latest delivered versions.

| IPF | IPF / Processing Baseline version | Date of deployment |
|---|---|---|
| S3A | | |
| SL1 | 06.21 / SL__L1_.004.06.00 | 25/07/2023 |
| SL2 LST | 06.21 / SL__LST.004.08.02 | 25/07/2023 |
| SL2 FRP (NTC) | 01.08 / FRP_NTC.004.08.02 | 25/07/2023 |

| IPF | IPF / Processing Baseline version | Date of deployment |
|---|---|---|
| S3B | | |
| SL1 | 06.21 / SL__L1_.004.06.00 | 18/07/2023 |
| SL2 LST | 06.21 / SL__LST.004.08.02 | 18/07/2023 |
| SL2 FRP (NTC) | 01.08 / FRP_NTC.004.08.02 | 18/07/2023 |

No deployment has been done this month.
The Processing Baselines of S3A and S3B are aligned with the latest processing baseline version.

## 2.2 Processing anomalies

No specific issue or evolutions has been identified this month on SLSTR.

There has been no major anomaly on data quality within the reported period.

# 3 Events and instrument anomalies

**Any events that have occurred in this month that cause significant data gaps and impact on quality are reported here.**

Some background to the typical events that might occur are provided below

- **RFI Radio Frequency Interference** occurs when another satellite causes the data downlink to the receiving station to be interrupted, and the data is lost.
- **Scheduled manoeuvres** may take place for Lunar views for calibration purposes, collision avoidance, or to maintain the nominal orbit. Will often result in the pointing flag being raised, and the geolocation accuracy is not nominal during this time.
- **Blackbody cross over tests** occur approximately once per year and the hot and cold blackbodies are swapped round for instrument testing.
- **De-icing** occurs when the instrument is heated to remove the build-up of ice.

## 3.1 SLSTR-A

SLSTR-A was switched on and operating nominally during November 2023, with Scan Unit Electronics (SUE) scanning and autonomous switching between day and night modes.

- 2nd November, 15:13 – 15:19 – Data gaps due to RFI
- 6th November, 21:48 – 21:54 – Data gaps due to RFI
- 9th November, 07:54 – 08:09 – Pointing flag raised dur tot In-Plane Manoeuvre
- 12th November, 03:08 – 03:11 – Data gaps
- 12th November, 08:47 – 08:53 – Data gaps due to RFI
- 13th November, 07:15 – 07:21 – Data gaps due to RFI
- 15th November, 23:51 – 00:06 – Data gaps
- 24th November, 21:39 – 21:45 – Data gaps
- 27th November, 05:54 – 06:00 – Data gaps due to RFI
- 27th November, 19:46 – 20:42 – Pointing flag and data gaps due to OLCI Moon Calibration

## 3.2 SLSTR-B

SLSTR-B was switched on and operating nominally during November 2023, with SUE scanning and autonomous switching between day and night modes.

- 1st November, 09:29 – 10:14 – Pointing flag raised due to In-Plane manoeuvre.
- 3rd November, 22:03 – 22:21 – Pointing flag raised due to In-Plane manoeuvre.
- 15th November, 09:35 – 09:50 – Pointing flag raised due to In-Plane manoeuvre.
- 16th November, 06:20 – 07:04 – Data gaps due to successive RFIs
- 17th November, 07:35 – 09:19 – Pointing flags and data gaps due to Collision avoidance manoeuvre
- 18th November, 14:20 – 14:26 – Data gaps due to RFI
- 21st November, 11:38 – 11:54; 16:39 – 16:48; 20:18 – 26:26 – Data gaps, cause still under investigation
- 24th November, 07:56 – 07:59; Data gaps

# 4 Instrument Status

**The health of the instrument impacts the data quality. This section contains in depth analysis of several instrument parameters over the month of operation, and in some cases, the latest annual and mission tends for context.**

SLSTR is a scanning radiometer, and uses two black bodies for thermal calibration, and a VISCAL unit for visible and shortwave IR calibration via the Sun. The key instrument properties that are monitored include:

- instrument temperature of the baffles
- instrument temperature of the Optical Mechanical Enclosure (optical bench, flip mirror and scan mirror, internal baffles)
- detector temperatures
- scanner and flip mirror performance

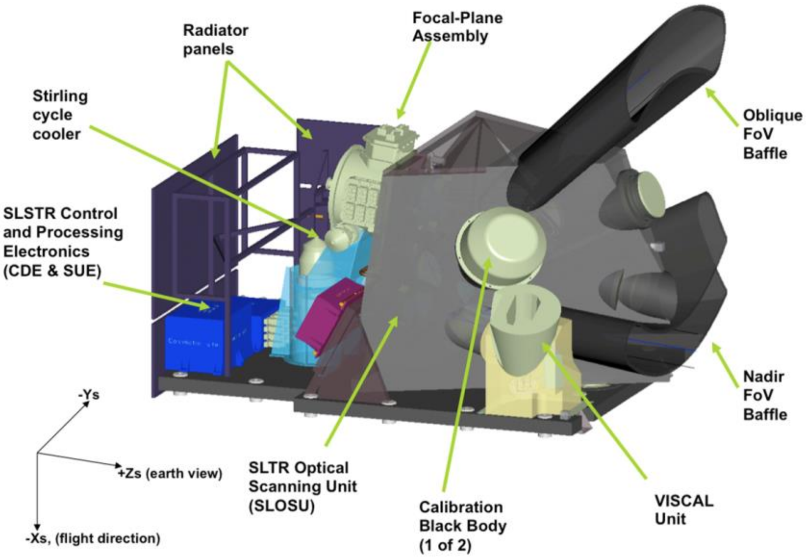

**Sentinel 3 A**

- The instrument was stable and compliant with requirements over much of the current month.

**Sentinel 3 B**

- The instrument was stable and compliant with requirements over the current month.

## 4.1 Instrument temperatures

As a thermal infrared instrument, thermal stability and uniformity of the optical mechanical enclosure (OME) is critical to the radiometric calibration. In this section we show the orbital average temperature of the OME and instrument baffles during the month. We expect to see a very small daily variation in temperature superimposed on a stable level over the month.

### 4.1.1 SLSTR-A

Figure 1 shows the orbital average temperature of the OME and instrument baffles for SLSTR-A during the month.

| OME Temperature over the last month | Baffle Temperature over the last month |
|---|---|
| 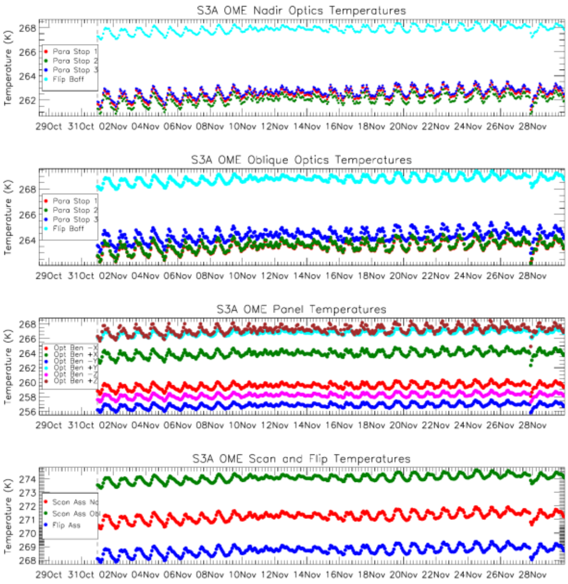 | 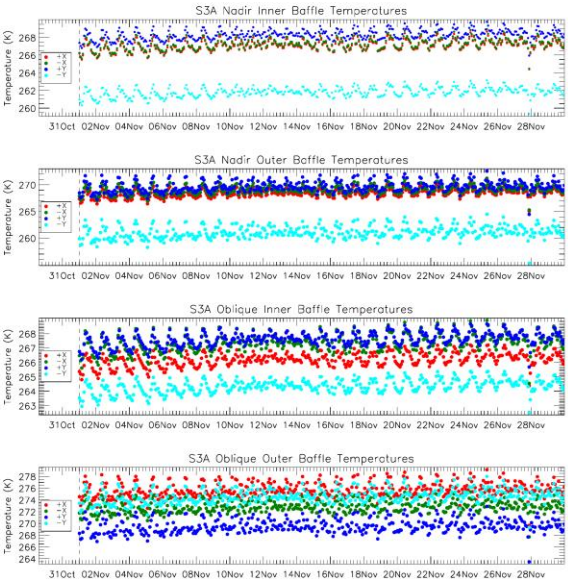 |

***Figure 1: OME temperature trends for SLSTR-A (left) and Baffle temperature trends (right) during November 2023. The OME plot shows the three paraboloid stops and flip baffle (top two plots) and optical bench at different positions (third plots), and scanner and flip assembly (bottom plots). The Baffle plot shows the temperature at different positions on the inner and outer baffles. Each dot represents the average temperature in one orbit.***

### 4.1.2 SLSTR-B

Figure 2 shows the orbital average temperature of the OME and instrument baffles for SLSTR-B during the month. The temperatures were stable (on top of a daily variation cycle).

| OME Temperature over the last month | Baffle Temperature over the last month |
|---|---|

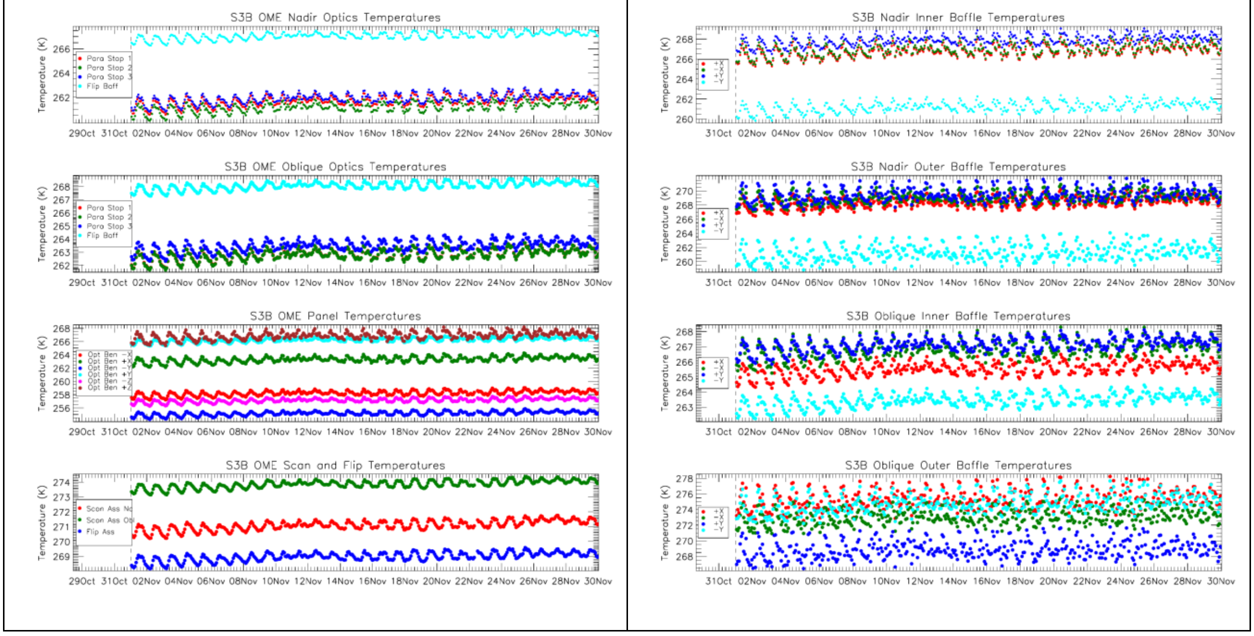

*Figure 2: SLSTR-B OME temperature trends (left) and Baffle temperature trends (right) during November 2023. The OME plot shows the three paraboloid stops and flip baffle (top two plots) and optical bench at different positions (third plots), and scanner and flip assembly (bottom plots). The Baffle plot shows the temperature at different positions on the inner and outer baffles. Each dot represents the average temperature in one orbit.*

## 4.2 Detector temperatures

The detector temperatures for both SLSTR-A and SLSTR-B were stable at their expected values over the month.

### 4.2.1 SLSTR-A

Figure 3 shows the annual trend in SLSTR-A detector temperatures for the past year. The temperatures from this month are consistent with the yearly trend.

**Detector Temperatures over the last year**

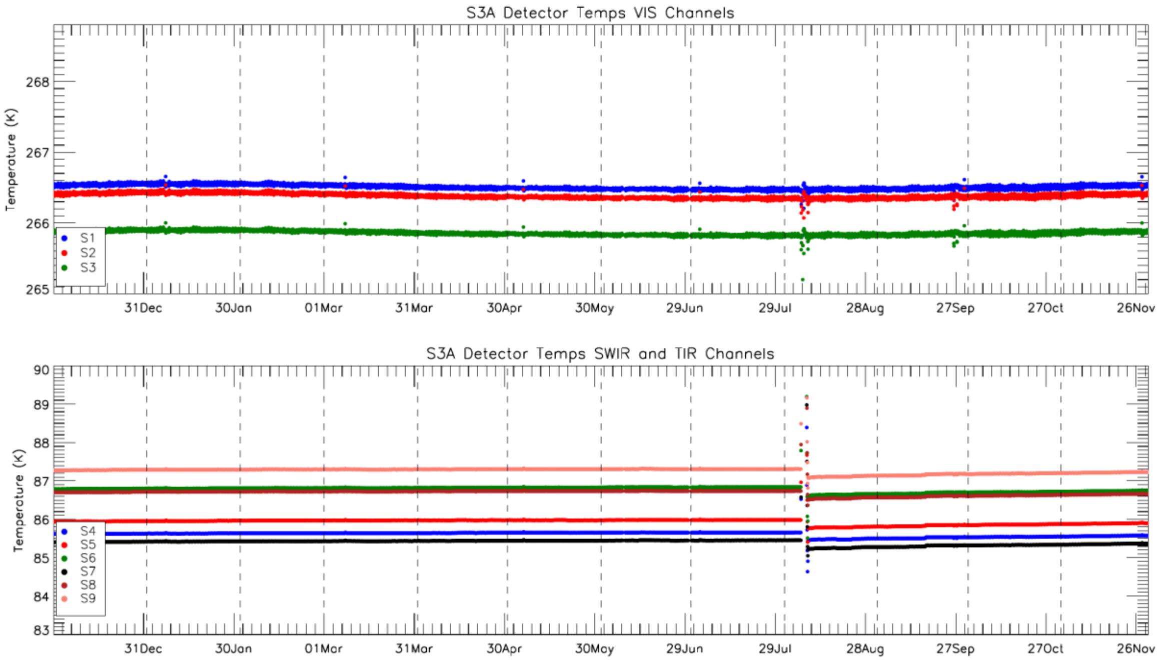

*Figure 3: SLSTR-A detector temperatures for each channel for the last month of operations. The vertical dashed lines indicate the start of each month. Each dot represents the average temperature in one orbit. The different colours indicate different detectors.*

### 4.2.2 SLSTR-B

Figure 4 shows the annual trend in SLSTR-B detector temperatures for the past year. The temperatures from this month are consistent with the yearly trend.

**Detector Temperatures over the last year**

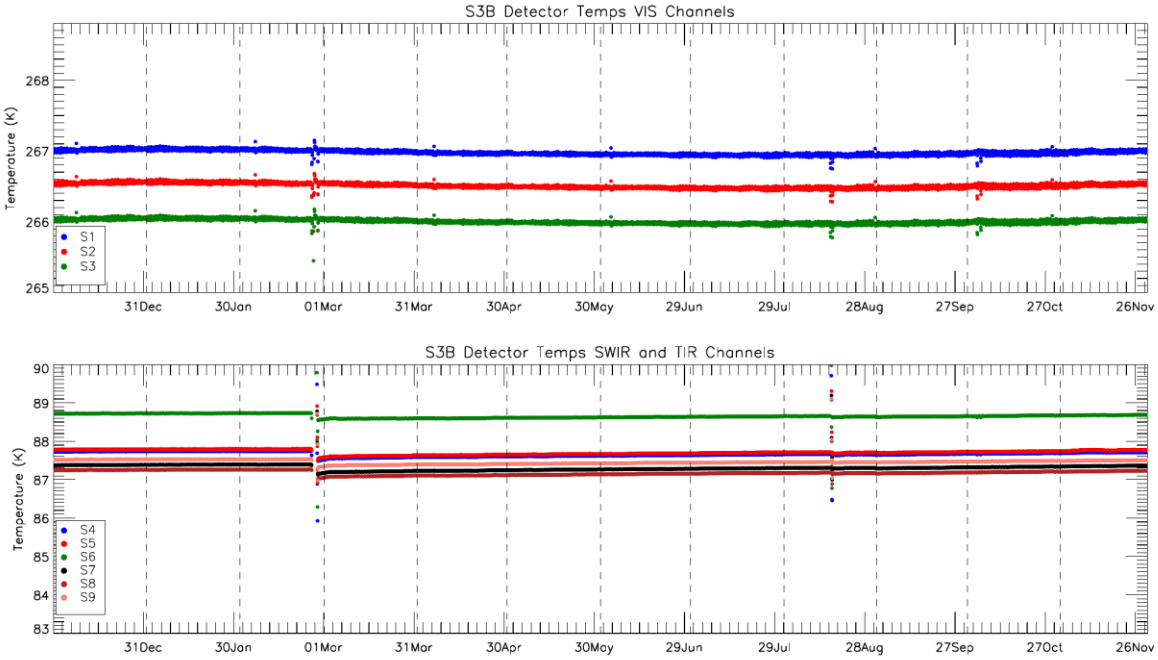

*Figure 4: SLSTR-B detector temperatures for each channel for the last month of operations. The vertical dashed lines indicate the start of each month. Each dot represents the average temperature in one orbit. The different colours indicate different detectors.*

## 4.3 Scanner performance

The actual position of the scan and flip mirrors is measured by the instrument, and in this section we show the statistics of the difference from the expected linear control law for each mirror in each view during November 2023. The performance has been consistent with previous operations and does not appear to be degrading. For reference, one arcsecond corresponds to roughly 4 m on the ground.

### 4.3.1 SLSTR-A

Figure 5 shows the statistics of the difference from the expected linear control law for each mirror in each view for SLSTR-A during the month.

| **Nadir view scanner and flip jitter** | **Oblique view scanner and flip jitter** |
|---|---|
| 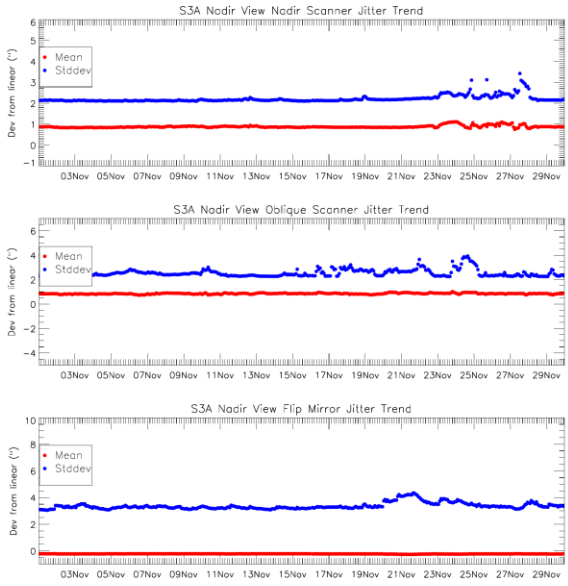 | 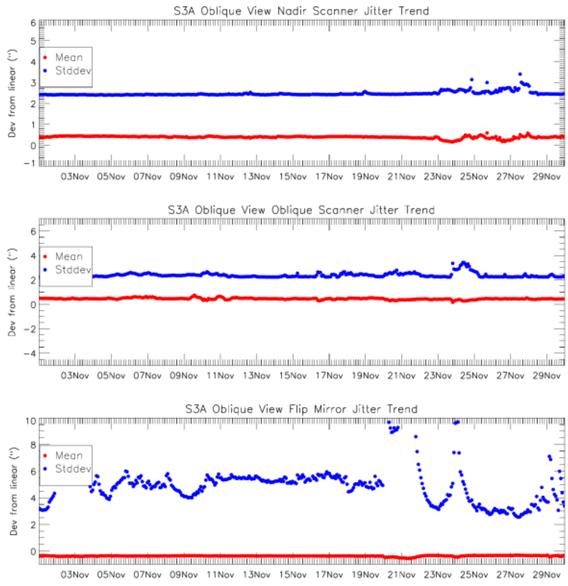 |

*Figure 5: SLSTR-A scanner and flip jitter for November 2023, showing mean and stddev from expected position per orbit (red and blue respectively) for the nadir view (left) and oblique view (right). The plots show the nadir scanner (top), oblique scanner (middle) and flip mirror (bottom).*

### 4.3.2 SLSTR-B

Figure 6 shows the statistics of the difference from the expected linear control law for each mirror in each view for SLSTR-B during the month.

| Nadir view scanner and flip jitter | Oblique view scanner and flip jitter |
|---|---|
| 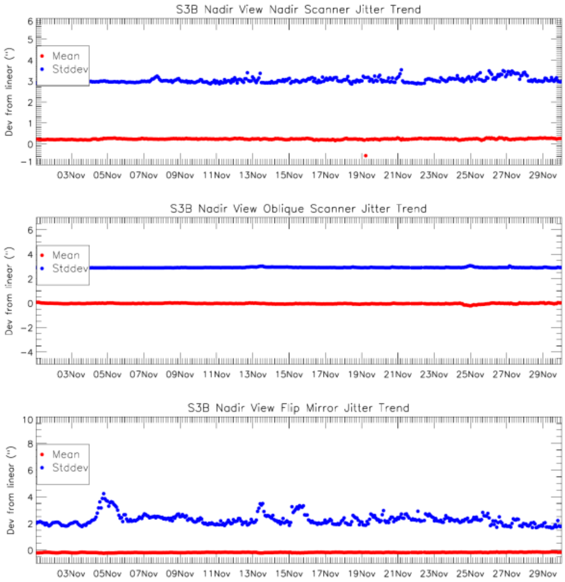 | 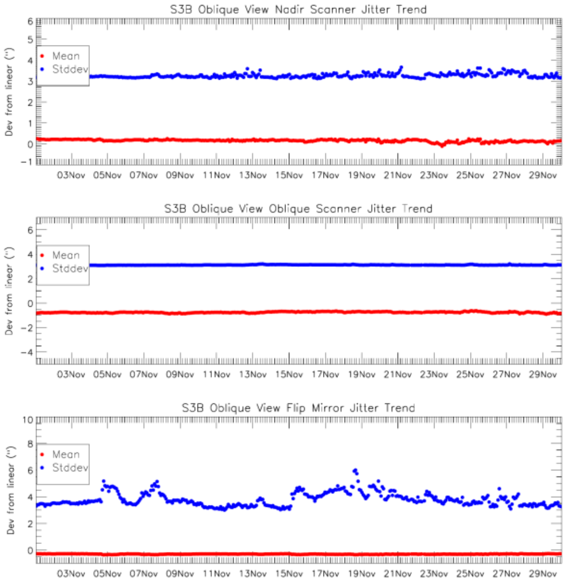 |

*Figure 6: SLSTR-B scanner and flip jitter for November 2023, showing mean and stddev difference from expected position per orbit (red and blue respectively) for the nadir view (left) and oblique view (right). The plots show the nadir scanner (top), oblique scanner (middle) and flip mirror (bottom).*

## 4.4 Black-Bodies

The monthly orbital average blackbody temperatures are shown in this section. The temperatures were stable on top of a daily variation cycle. There are also longer term trends which show a yearly variation, with temperatures rising as the Earth approaches perihelion at the beginning of January – this variation is shown in the monthly averages in Figure 7 and Table 5.

**Latest mission trend of +Y hot BB temperature**

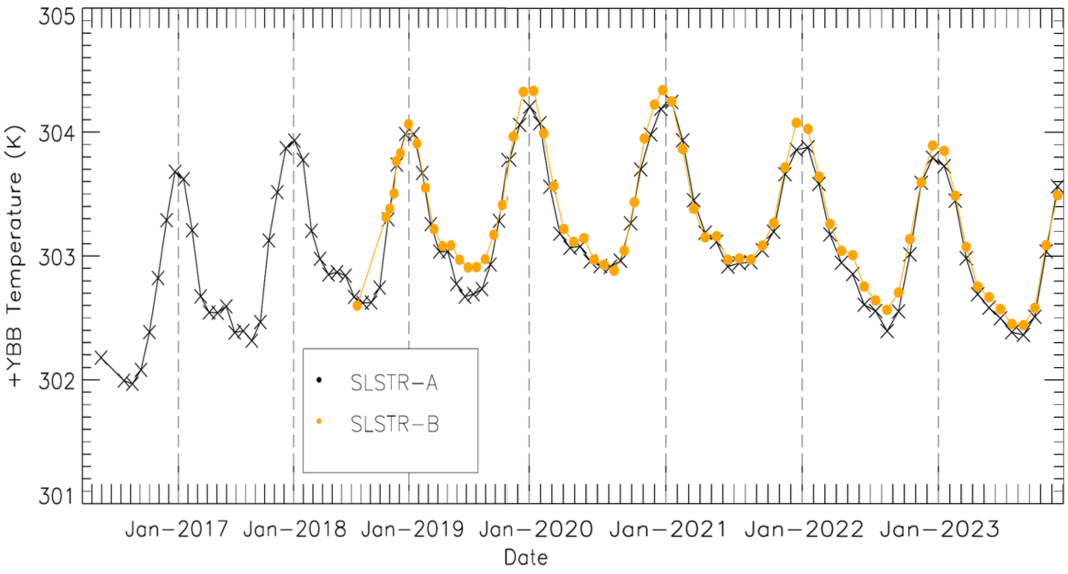

*Figure 7: SLSTR-A and SLSTR-B long term trends in average +YBB temperature, showing yearly variation. The vertical dashed lines indicate the 1st January in each year.*

### 4.4.1 SLSTR-A

The monthly orbital average blackbody temperatures for SLSTR-A are shown in Figure 8. The temperatures were stable on top of a daily variation cycle. Figure 8 also shows the gradients across the blackbody baseplate (i.e., each Platinum Resistance Thermometer (PRT) sensor reading relative to the mean). The gradients are stable and within their expected range of ±20mK.

**Blackbody temperature over the month**

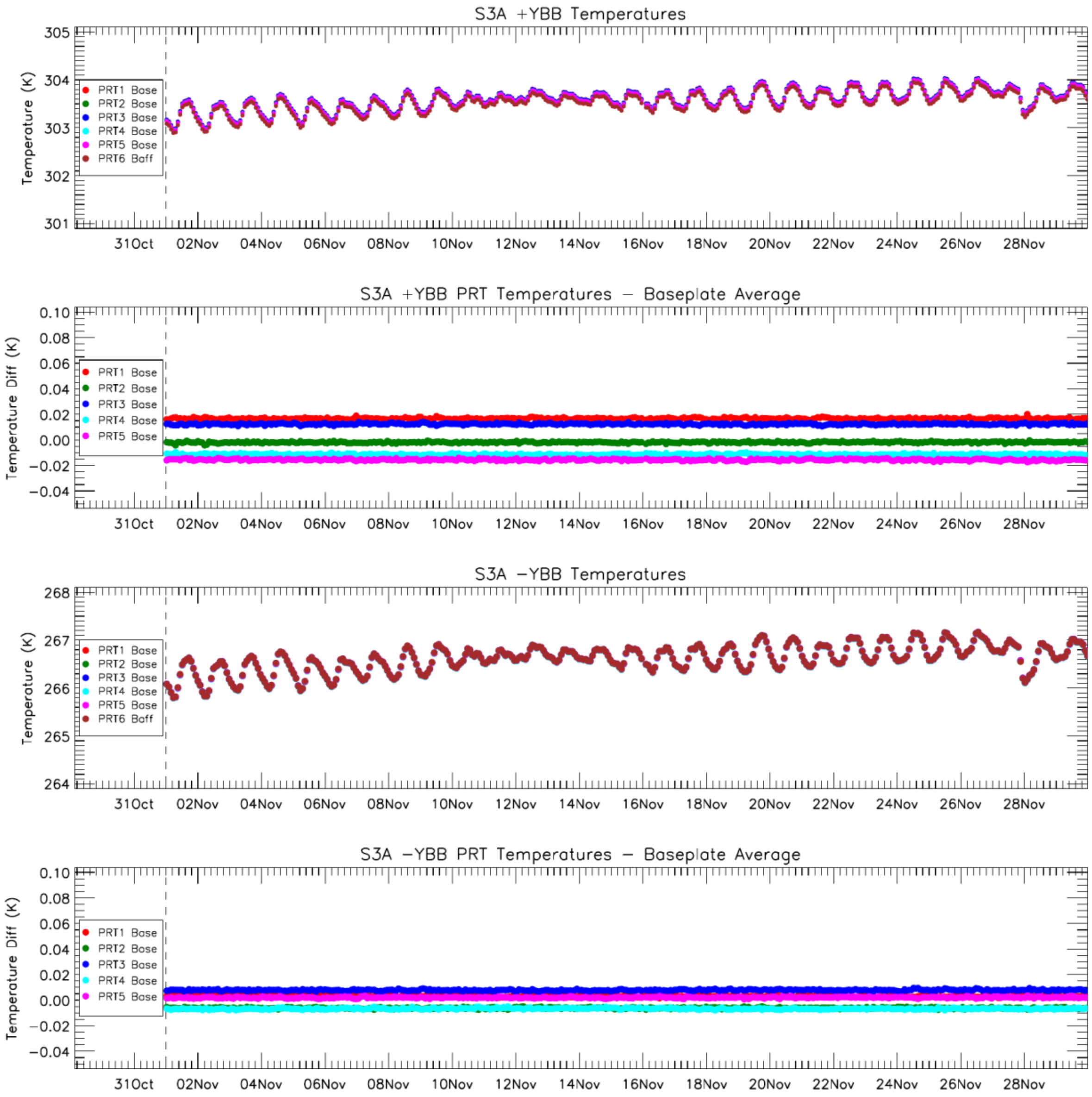

*Figure 8: SLSTR-A blackbody temperature and baseplate gradient trends during November 2023 measured by different sensors at various positions in the BB and Baseplate. Each dot represents the average temperature in one orbit.*

### 4.4.2 SLSTR-B

The monthly orbital average blackbody temperatures for SLSTR-B are shown in Figure 9. The temperatures were stable on top of a daily variation cycle. Figure 9 also shows the gradients across the blackbody baseplate (i.e., each Platinum Resistance Thermometer (PRT) sensor reading relative to the mean). The gradients are stable and within their expected range of ±20mK, except for the +Y blackbody for SLSTR-B which has a higher gradient. This higher gradient is expected and consistent with measurements made before launch.

**Blackbody temperature over the month**

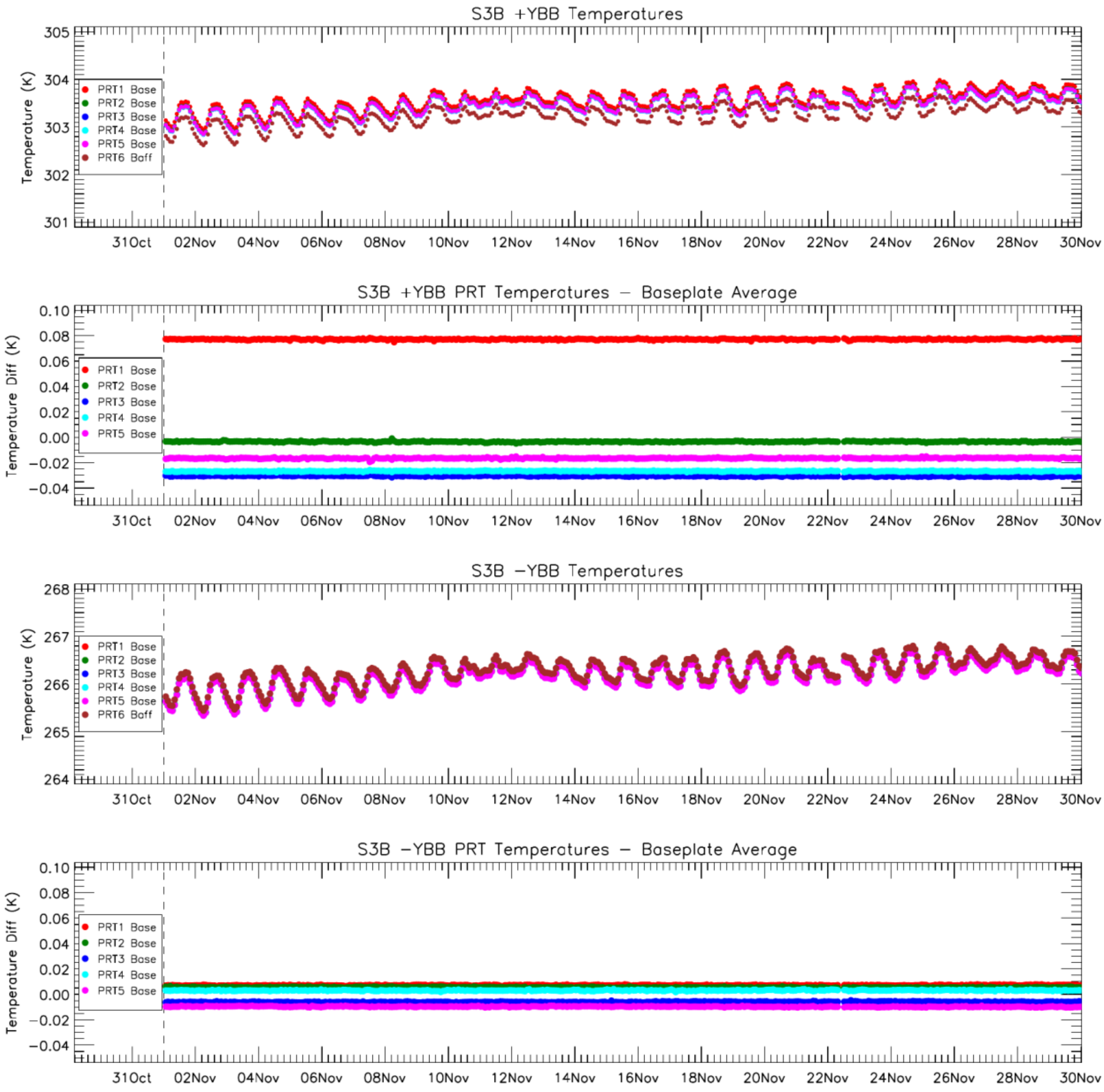

*Figure 9: SLSTR-B blackbody temperature and baseplate gradient trends during November 2023 measured by different sensors at various positions in the BB and Baseplate. Each dot represents the average temperature in one orbit.*

## 4.5 Detector noise levels

### 4.5.1 SLSTR-A VIS and SWIR channel signal-to-noise

The VIS and SWIR channel noise for SLSTR-A during November 2023 was stable and consistent with previous operations - the signal-to-noise ratio of the measured VISCAL signal over the past year is plotted in Figure 10 and Figure 11. Table 1 and Table 2 give the average monthly signal-to-noise (excluding the instrument decontaminations). These values average over the significant detector-detector dispersion for the SWIR channels that is shown in Figure 11. Note that these averages are now calculated for each calendar month, whereas in data quality reports before January 2022 they were aligned to the satellite 27 day repeat cycles.

*Table 1: Average SLSTR-A reflectance factor, and signal-to-noise ratio of the measured VISCAL signal for the last 11 months, averaged over all detectors for the nadir view.*

| | Average Reflectance Factor | Jan 2023 | Feb 2023 | Mar 2023 | Apr 2023 | May 2023 | Jun 2023 | Jul 2023 | Aug 2023 | Sep 2023 | Oct 2023 | Nov 2023 |
|---|---|---|---|---|---|---|---|---|---|---|---|---|
| **S1** | 0.187 | 239 | 239 | 242 | 244 | 239 | 234 | 235 | 238 | 236 | 243 | 246 |
| **S2** | 0.194 | 246 | 243 | 241 | 243 | 243 | 242 | 241 | 242 | 241 | 243 | 245 |
| **S3** | 0.190 | 231 | 229 | 225 | 223 | 218 | 213 | 216 | 222 | 221 | 222 | 223 |
| **S4** | 0.191 | 174 | 172 | 171 | 170 | 166 | 164 | 164 | 168 | 171 | 173 | 174 |
| **S5** | 0.193 | 291 | 289 | 284 | 283 | 280 | 280 | 279 | 280 | 283 | 285 | 287 |
| **S6** | 0.175 | 187 | 185 | 183 | 181 | 180 | 178 | 178 | 181 | 183 | 184 | 186 |

*Table 2: Average SLSTR-A reflectance factor, and signal-to-noise ratio of the measured VISCAL signal for the last 11 months, averaged over all detectors for the oblique view.*

| | Average Reflectance Factor | Jan 2023 | Feb 2023 | Mar 2023 | Apr 2023 | May 2023 | Jun 2023 | Jul 2023 | Aug 2023 | Sep 2023 | Oct 2023 | Nov 2023 |
|---|---|---|---|---|---|---|---|---|---|---|---|---|
| **S1** | 0.166 | 259 | 259 | 262 | 261 | 252 | 242 | 246 | 250 | 249 | 256 | 265 |
| **S2** | 0.170 | 268 | 262 | 260 | 258 | 255 | 250 | 256 | 257 | 256 | 259 | 264 |
| **S3** | 0.168 | 238 | 235 | 232 | 226 | 219 | 213 | 217 | 222 | 222 | 222 | 223 |
| **S4** | 0.166 | 139 | 138 | 138 | 138 | 137 | 134 | 136 | 138 | 139 | 139 | 140 |
| **S5** | 0.166 | 211 | 209 | 214 | 214 | 214 | 208 | 213 | 213 | 215 | 215 | 217 |
| **S6** | 0.155 | 131 | 129 | 131 | 131 | 131 | 130 | 129 | 132 | 134 | 134 | 137 |

## VIS channels SNR over the last year

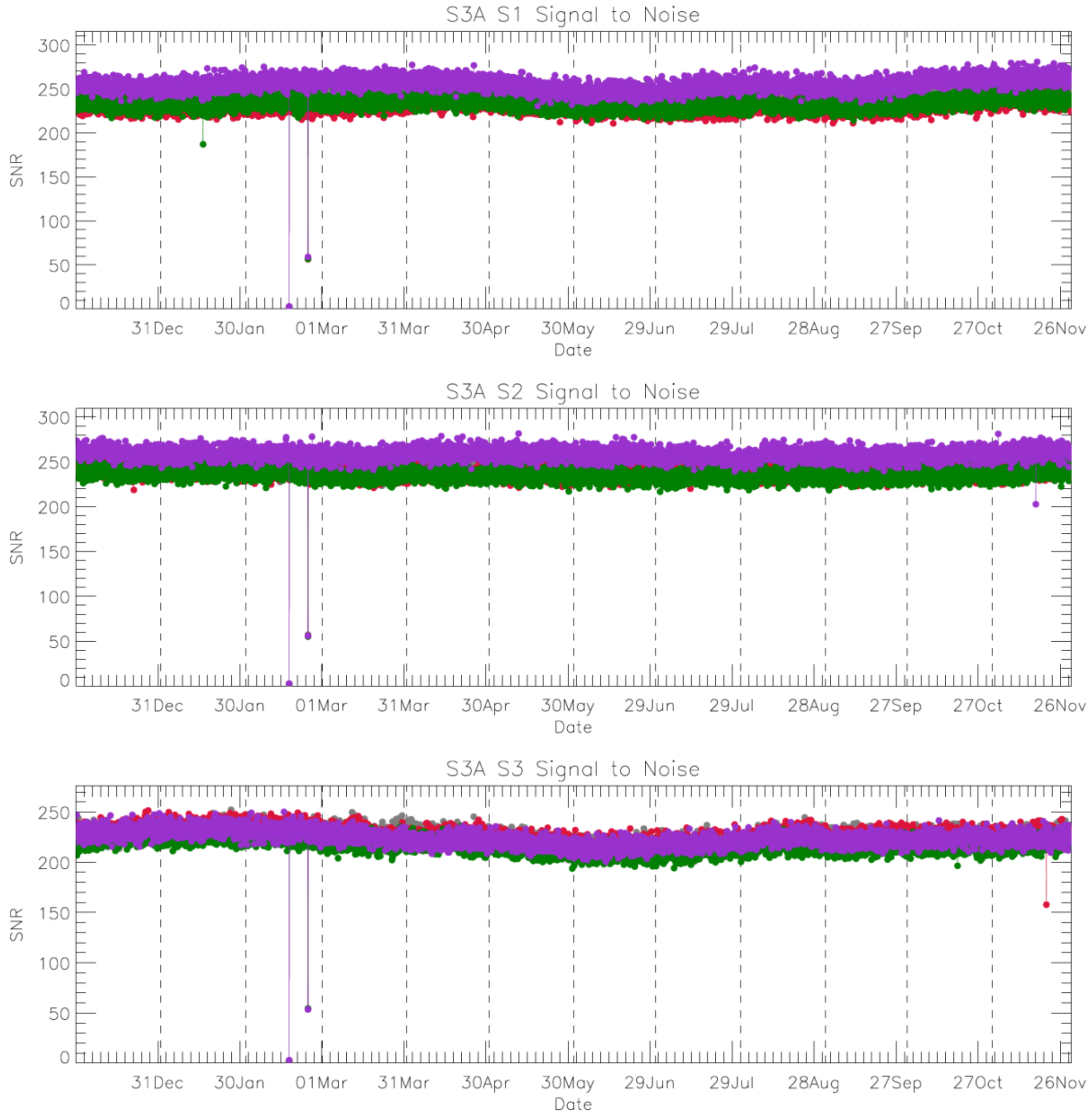

*Figure 10: VIS channel signal-to-noise of the measured VISCAL signal in each orbit for the last year of operations for SLSTR-A. Different colours indicate different detectors. The vertical dashed lines indicate the start of each month.*

## SWIR SNR over the last year

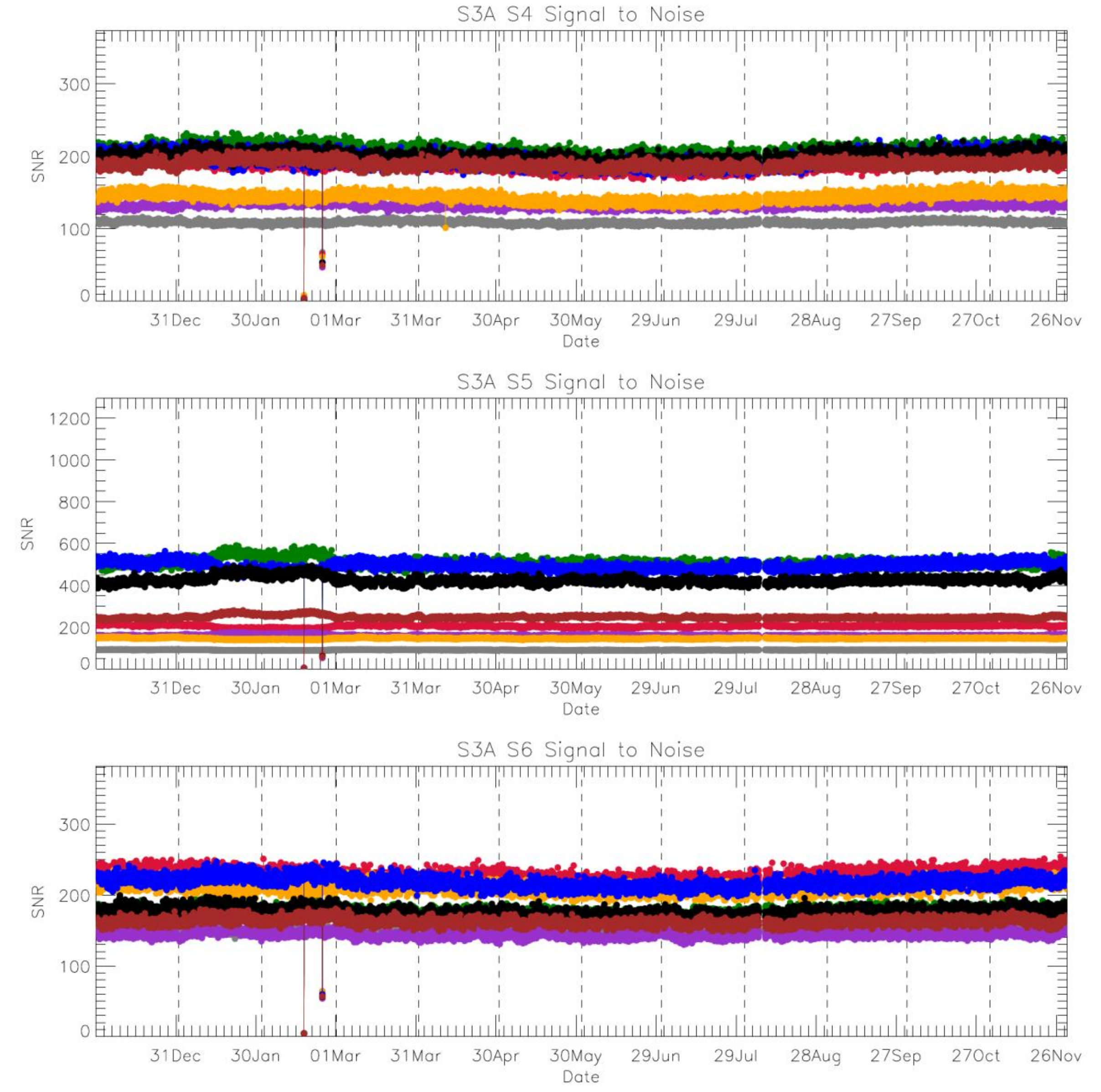

***Figure 11. SWIR channel signal-to-noise of the measured VISCAL signal in each orbit for the last year of operations for SLSTR-A. Different colours indicate different detectors. The vertical dashed lines indicate the start of each month.***

### 4.5.2 SLSTR-B VIS and SWIR channel signal-to-noise

The monthly average VIS and SWIR channel signal-to-noise ratios for SLSTR-B are shown in Table 3 and Table 4. These values average over a significant detector-detector dispersion for the SWIR channels.

***Table 3: Average SLSTR-B reflectance factor, and signal-to-noise ratio of the measured VISCAL signal for the last 11 months, averaged over all detectors for the nadir view.***

| | Average Reflectance Factor | Jan 2023 | Feb 2023 | Mar 2023 | Apr 2023 | May 2023 | Jun 2023 | Jul 2023 | Aug 2023 | Sep 2023 | Oct 2023 | Nov 2023 |
|---|---|---|---|---|---|---|---|---|---|---|---|---|
| **S1** | 0.177 | 238 | 238 | 223 | 227 | 228 | 221 | 219 | 226 | 232 | 231 | 228 |
| **S2** | 0.192 | 221 | 221 | 218 | 215 | 214 | 216 | 214 | 215 | 217 | 221 | 225 |
| **S3** | 0.194 | 223 | 226 | 222 | 217 | 213 | 214 | 216 | 219 | 219 | 219 | 218 |
| **S4** | 0.186 | 131 | 130 | 129 | 129 | 128 | 126 | 126 | 126 | 127 | 127 | 128 |
| **S5** | 0.184 | 242 | 243 | 243 | 240 | 239 | 238 | 237 | 238 | 238 | 239 | 242 |
| **S6** | 0.162 | 165 | 165 | 162 | 161 | 159 | 159 | 157 | 159 | 158 | 158 | 162 |

***Table 4: Average SLSTR-B reflectance factor, and signal-to-noise ratio of the measured VISCAL signal for the last 11 months, averaged over all detectors for the oblique view.***

| | Average Reflectance Factor | Jan 2023 | Feb 2023 | Mar 2023 | Apr 2023 | May 2023 | Jun 2023 | Jul 2023 | Aug 2023 | Sep 2023 | Oct 2023 | Nov 2023 |
|---|---|---|---|---|---|---|---|---|---|---|---|---|
| **S1** | 0.157 | 228 | 222 | 217 | 219 | 217 | 208 | 208 | 216 | 220 | 217 | 218 |
| **S2** | 0.168 | 256 | 255 | 251 | 245 | 245 | 245 | 241 | 242 | 246 | 255 | 258 |
| **S3** | 0.172 | 253 | 253 | 248 | 237 | 232 | 234 | 238 | 239 | 238 | 238 | 240 |
| **S4** | 0.168 | 132 | 131 | 131 | 130 | 127 | 124 | 126 | 126 | 128 | 128 | 128 |
| **S5** | 0.172 | 251 | 251 | 251 | 251 | 249 | 248 | 248 | 247 | 249 | 249 | 252 |
| **S6** | 0.152 | 188 | 186 | 188 | 187 | 182 | 180 | 180 | 182 | 184 | 185 | 188 |

### VIS channels SNR over the last year

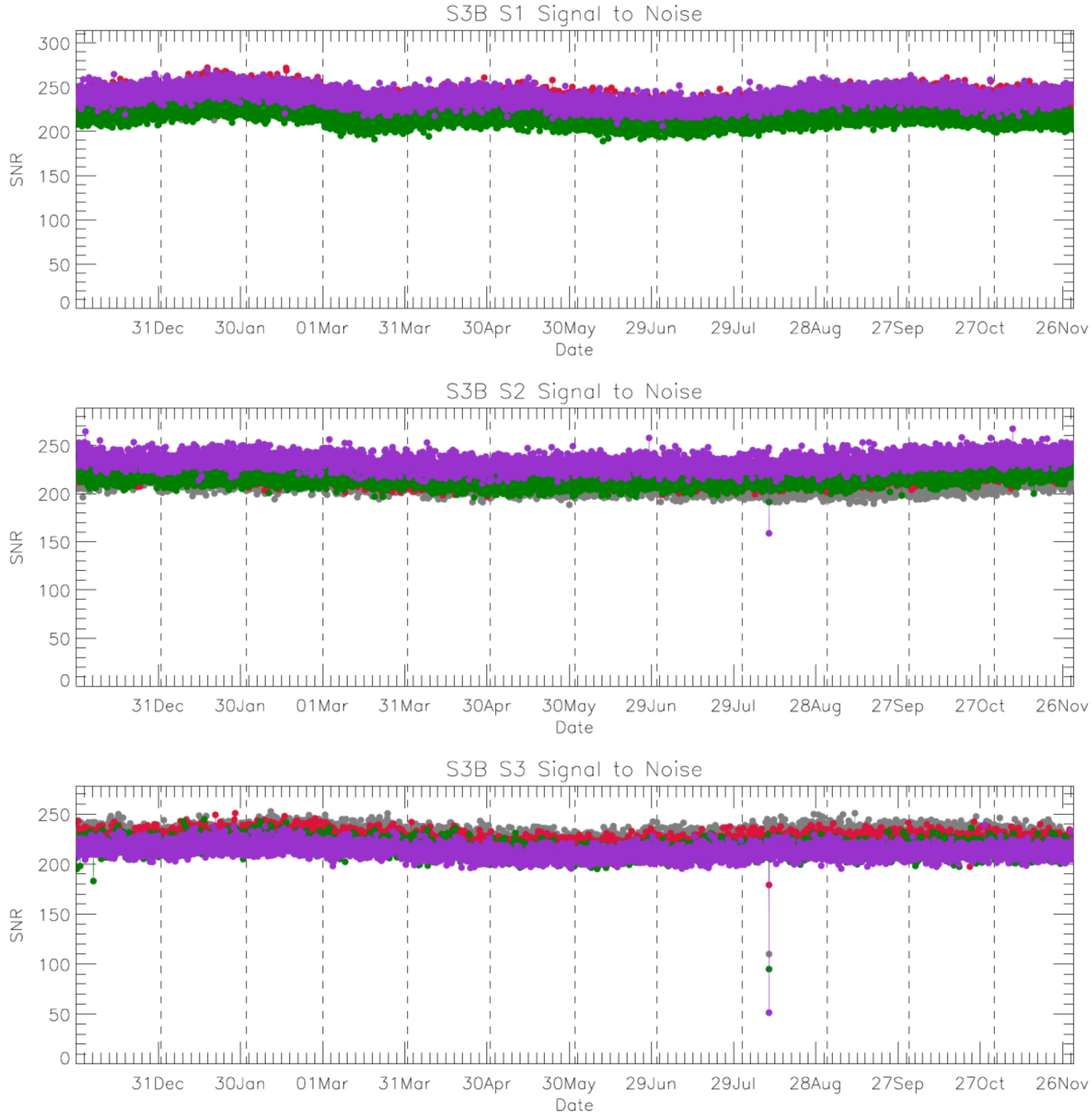

***Figure 12: VIS channel signal-to-noise of the measured VISCAL signal in each orbit for the last year of operations for SLSTR-B. Different colours indicate different detectors. The vertical dashed lines indicate the start of each month.***

**SWIR SNR over the last year**

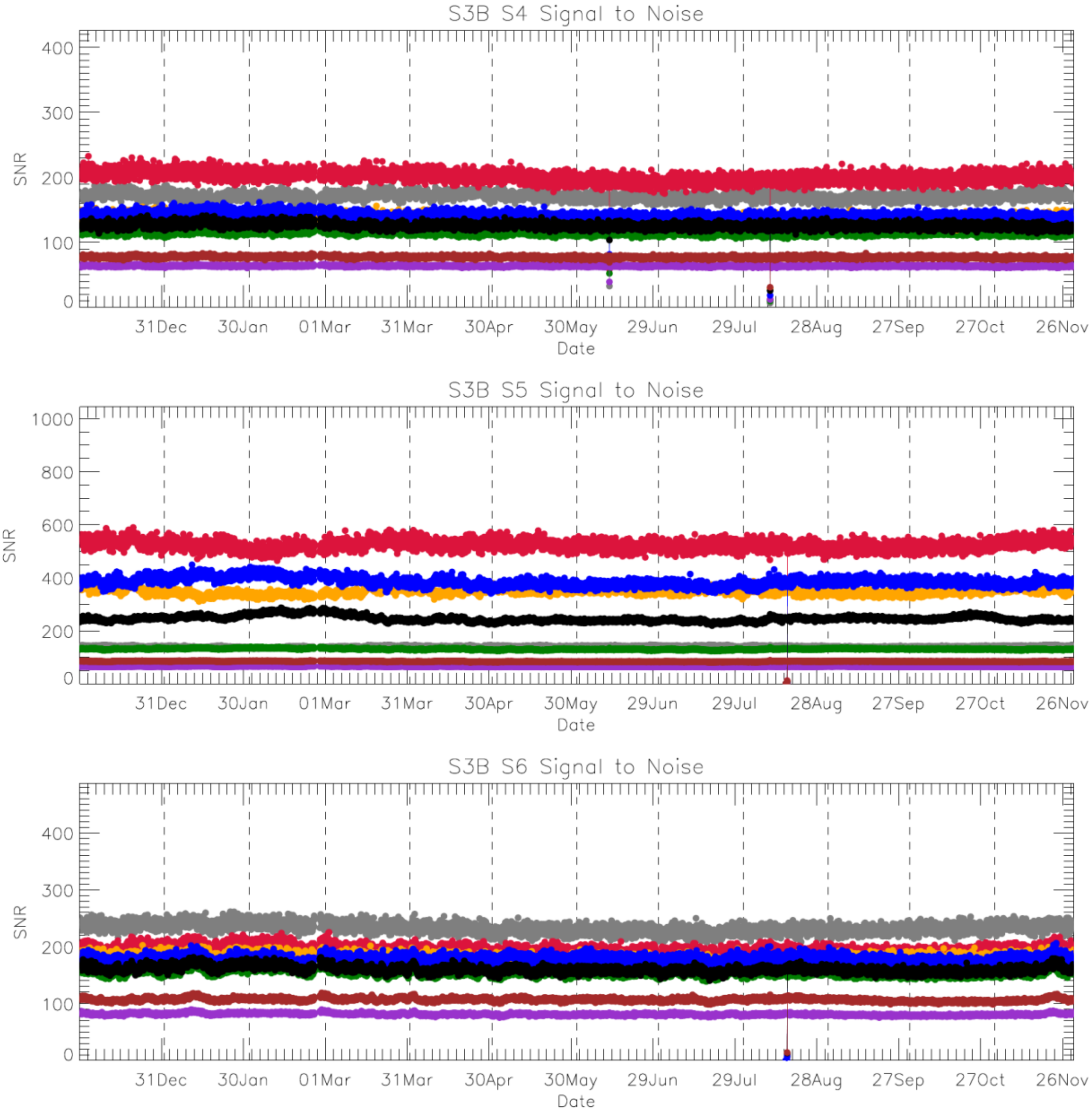

*Figure 13. SWIR channel signal-to-noise of the measured VISCAL signal in each orbit for the last year of operations for SLSTR-B. Different colours indicate different detectors. The vertical dashed lines indicate the start of each month.*

### 4.5.3 SLSTR-A TIR channel NEDT

The thermal channel NEDT values for SLSTR-A in November 2023 are consistent with previous operations and within the requirements. NEDT trends calculated from the hot and cold blackbody signals are shown in Figure 14. Monthly NEDT values, averaged over all detectors and both Earth views, are shown in Table 5.

**TIR NEDT over the month**

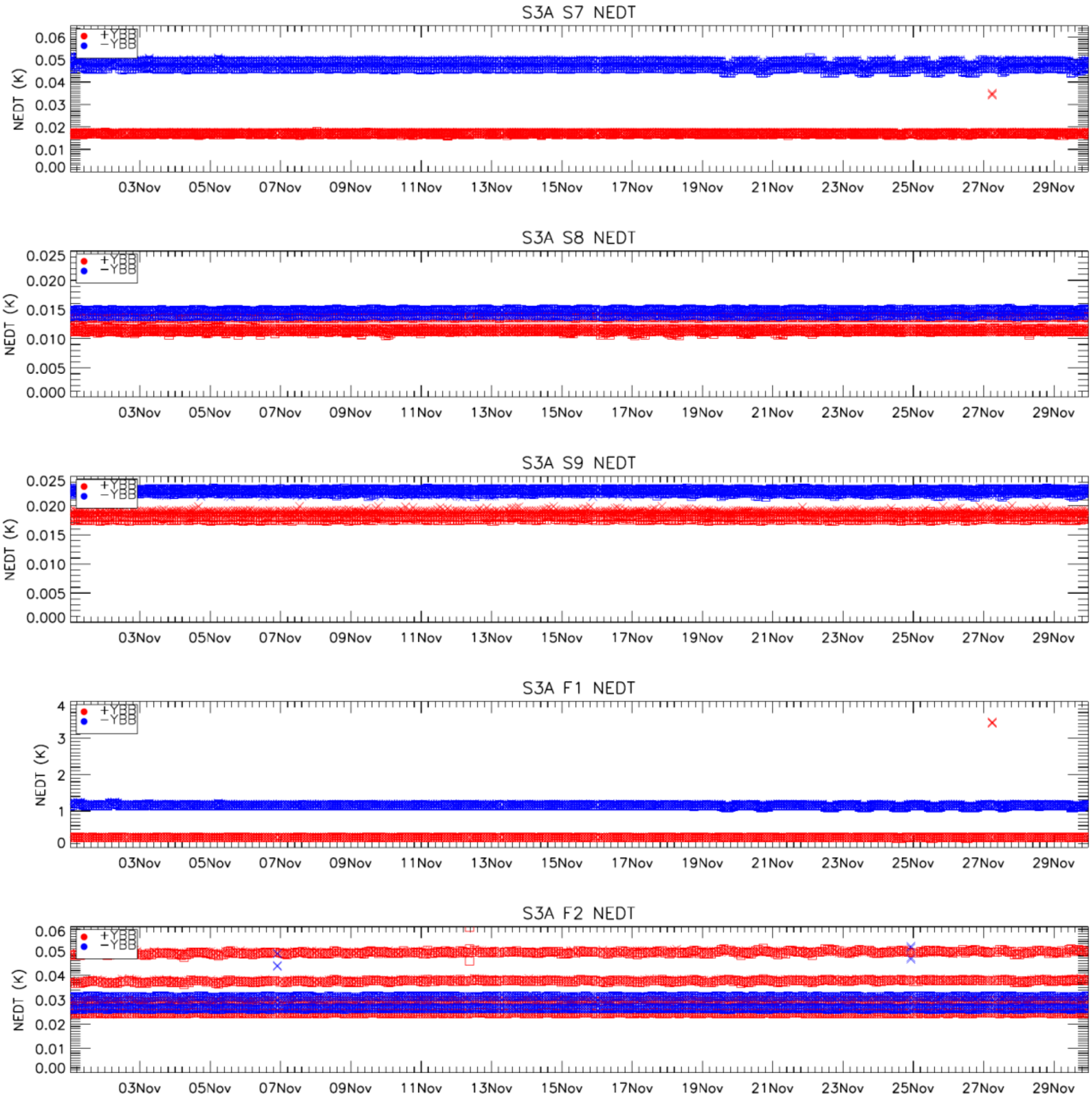

*Figure 14: SLSTR-A NEDT trend for the thermal channels in November 2023. Blue points were calculated from the cold blackbody signal and red points from the hot blackbody. The square symbols show results calculated from the nadir view and crosses show results from the oblique view. Results are plotted for all detectors and integrators, which is why there are several different levels within the same colour points (particularly for S8 and F2).*

*Table 5: NEDT for SLSTR-A in the last 11 months averaged over all detectors for both Earth views towards the hot +YBB (top) and the cold -YBB (bottom).*

| SLSTR-A | | Jan 2023 | Feb 2023 | Mar 2023 | Apr 2023 | May 2023 | June 2023 | July 2023 | Aug 2023 | Sep 2023 | Oct 2023 | Nov 2023 |
|---|---|---|---|---|---|---|---|---|---|---|---|---|
| +YBB temp (K) | | 303.727 | 303.447 | 302.983 | 302.692 | 302.584 | 302.498 | 302.385 | 302.363 | 302.514 | 303.038 | 303.562 |
| NEDT (mK) | S7 | 17.2 | 17.2 | 17.4 | 17.6 | 17.6 | 17.6 | 17.6 | 17.5 | 18.1 | 17.3 | 17.2 |
| | S8 | 12.0 | 12.0 | 12.0 | 12.1 | 12.1 | 12.1 | 12.1 | 11.9 | 12.0 | 11.9 | 12 |
| | S9 | 18.5 | 18.5 | 18.5 | 18.6 | 18.6 | 18.6 | 18.7 | 18.3 | 18.4 | 18.3 | 18.3 |
| | F1 | 279 | 279 | 284 | 288 | 290 | 290 | 290 | 284 | 302 | 281 | 282 |
| | F2 | 35.3 | 35.3 | 34.9 | 34.8 | 34.7 | 34.6 | 34.6 | 34.5 | 34.5 | 34.9 | 35.4 |

| SLSTR-A | | Jan 2023 | Feb 2023 | Mar 2023 | Apr 2023 | May 2023 | June 2023 | July 2023 | Aug 2023 | Sep 2023 | Oct 2023 | Nov 2023 |
|---|---|---|---|---|---|---|---|---|---|---|---|---|
| -YBB temp (K) | | 266.695 | 266.319 | 265.801 | 265.594 | 265.630 | 265.589 | 265.224 | 265.201 | 265.299 | 265.941 | 266.571 |
| NEDT (mK) | S7 | 48.0 | 48.5 | 49.4 | 50.1 | 50.4 | 50.2 | 49.8 | 49.8 | 48.3 | 48.7 | 47.7 |
| | S8 | 14.6 | 14.6 | 14.7 | 14.7 | 14.7 | 14.7 | 14.7 | 14.6 | 14.5 | 14.6 | 14.6 |
| | S9 | 22.7 | 22.7 | 22.8 | 22.9 | 23.0 | 23 | 23.1 | 22.6 | 22.4 | 22.5 | 22.5 |
| | F1 | 1169 | 1186 | 1218 | 1236 | 1245 | 1247 | 1243 | 1219 | 1187 | 1195 | 1177 |
| | F2 | 28.9 | 28.9 | 28.9 | 29.0 | 29.1 | 29.0 | 29.0 | 28.7 | 29.0 | 28.8 | 28.9 |

### 4.5.4 SLSTR-B TIR channel NEDT

The thermal channel NEDT values for SLSTR-B in November 2023, calculated from the hot and cold blackbody signals are shown in Figure 15 with monthly averages in Table 6. The thermal channel NEDT values for SLSTR-B in November 2023 are consistent with previous operations and within the requirements. Note that these averages are now calculated for each calendar month, whereas in data quality reports before January 2022 they were aligned to the satellite 27-day repeat cycles.

## TIR NEDT over the month

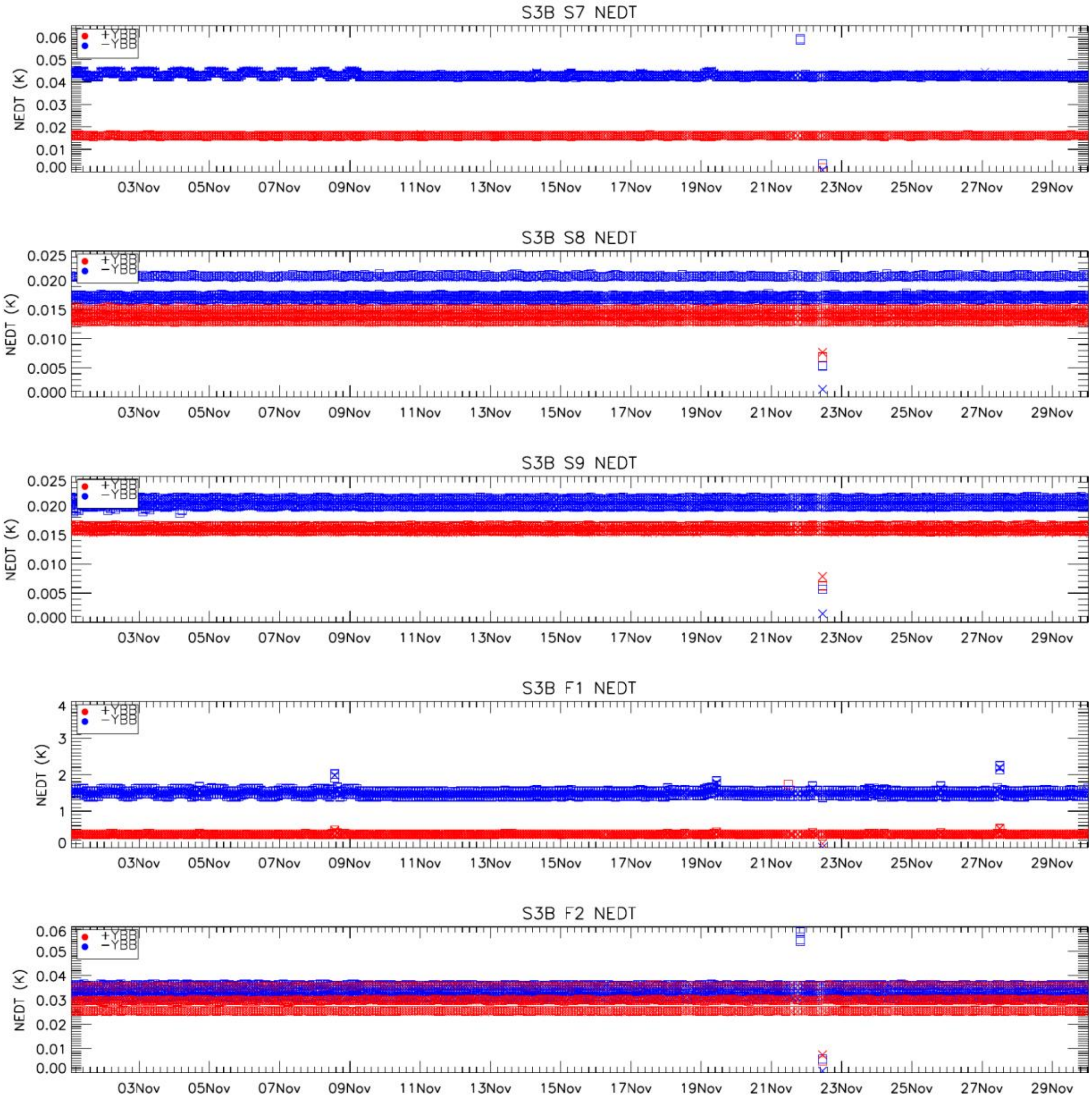

*Figure 15: SLSTR-B NEDT trend for the thermal channels in November 2023. Blue points were calculated from the cold blackbody signal and red points from the hot blackbody. The square symbols show results calculated from the nadir view and crosses show results from the oblique view. Results are plotted for all detectors and integrators, which is why there are several different levels within the same colour points (particularly for S8 and F2).*

*Table 6: NEDT for SLSTR-B in the last 11 months averaged over all detectors for both Earth views towards the hot +YBB (top) and the cold -YBB (bottom).*

| SLSTR-B | | Jan 2023 | Feb 2023 | Mar 2023 | Apr 2023 | May 2023 | Jun 2023 | Jul 2023 | Aug 2023 | Sep 2023 | Oct 2023 | Nov 2023 |
|---|---|---|---|---|---|---|---|---|---|---|---|---|
| +YBB temp (K) | | 303.850 | 303.489 | 303.074 | 302.754 | 302.668 | 302.572 | 302.452 | 302.442 | 302.582 | 303.582 | 303.492 |
| NEDT (mK) | S7 | 16.0 | 16.1 | 16.2 | 16.5 | 16.5 | 16.5 | 16.5 | 16.5 | 16.5 | 16.8 | 16.1 |
| | S8 | 13.9 | 14.0 | 14.0 | 14.0 | 14.0 | 14.0 | 14.1 | 14.1 | 14.0 | 14.1 | 13.9 |
| | S9 | 15.9 | 16.0 | 15.8 | 15.8 | 15.9 | 15.9 | 16.0 | 16.0 | 16.0 | 16.1 | 16.0 |
| | F1 | 349 | 369 | 367 | 368 | 367 | 369 | 374 | 378 | 380 | 393 | 369 |
| | F2 | 30.5 | 30.4 | 30.2 | 30.3 | 30.3 | 30.2 | 30.1 | 30.1 | 30.1 | 30.2 | 30.3 |

| SLSTR-B | | Jan 2023 | Feb 2023 | Mar 2023 | Apr 2023 | May 2023 | Jun 2023 | Jul 2023 | Aug 2023 | Sep 2023 | Oct 2023 | Nov 2023 |
|---|---|---|---|---|---|---|---|---|---|---|---|---|
| -YBB temp (K) | | 266.431 | 265.924 | 265.360 | 265.131 | 265.196 | 265.146 | 264.944 | 264.837 | 264.943 | 265.568 | 266.185 |
| NEDT (mK) | S7 | 42.8 | 43.7 | 44.6 | 44.5 | 44.3 | 44.8 | 45.5 | 45.9 | 45.3 | 42.3 | 43.0 |
| | S8 | 18.0 | 18.0 | 17.8 | 17.8 | 17.9 | 17.9 | 18.0 | 18.0 | 18.0 | 17.8 | 18.0 |
| | S9 | 20.4 | 20.5 | 20.2 | 20.3 | 20.3 | 20.4 | 20.4 | 20.5 | 20.5 | 20.3 | 20.4 |
| | F1 | 1430 | 1564 | 1550 | 1525 | 1502 | 1529 | 1571 | 1592 | 1595 | 1503 | 1501 |
| | F2 | 33.2 | 33.3 | 33.1 | 33.1 | 33.2 | 33.3 | 33.4 | 33.4 | 33.3 | 33.1 | 33.1 |

## 4.6 Calibration factors

### 4.6.1 VIS and SWIR radiometric response

The radiometric gain derived from the VISCAL signals over the past year are shown in this section. It should be noted that the data from the VISCAL unit and blackbodies calibrates the signal and counteracts the degradation of the optics and other variations in signal observed in the plots.

There are several features that appear in this parameter that can be explained as:

- The visible channels show oscillations in their radiometric response due to the build-up of ice on the optical path within the focal plane assembly (FPA). Similar oscillations were observed for the corresponding channels on ATSR-2 and AATSR. As described in Section 4.2, periodic decontamination of the infrared FPA is necessary to remove the water ice contamination.
- The radiometric responses of the SWIR channels appear to be more stable and not affected by the build-up of water ice contamination, although there is a seasonal cycle of the response that could be caused by variations in the solar zenith angle on the diffuser or partial vignetting of the Sun's disc by the VISCAL baffle.
- Note that the period of the oscillations depends on the rate of build up of the ice layer, which is faster for SLSTR-B because it has had less time to decontaminate.

### 4.6.2 SLSTR-A

Figure 16 and Figure 17 show the variation of the radiometric gain derived from the VISCAL signals for SLSTR-A over the past year. The data from the last month appears normal and follows the expected trend. The following features in this annual trend plot should be noted:

- August 2023: an anomaly occurred on the instrument on 6th August, which was recovered with a power cycle and decontamination/cooldown. This causes a discontinuity in the gain due to the reduction in water ice after the decontamination.

**VIS VISCAL signal variation over the past year**

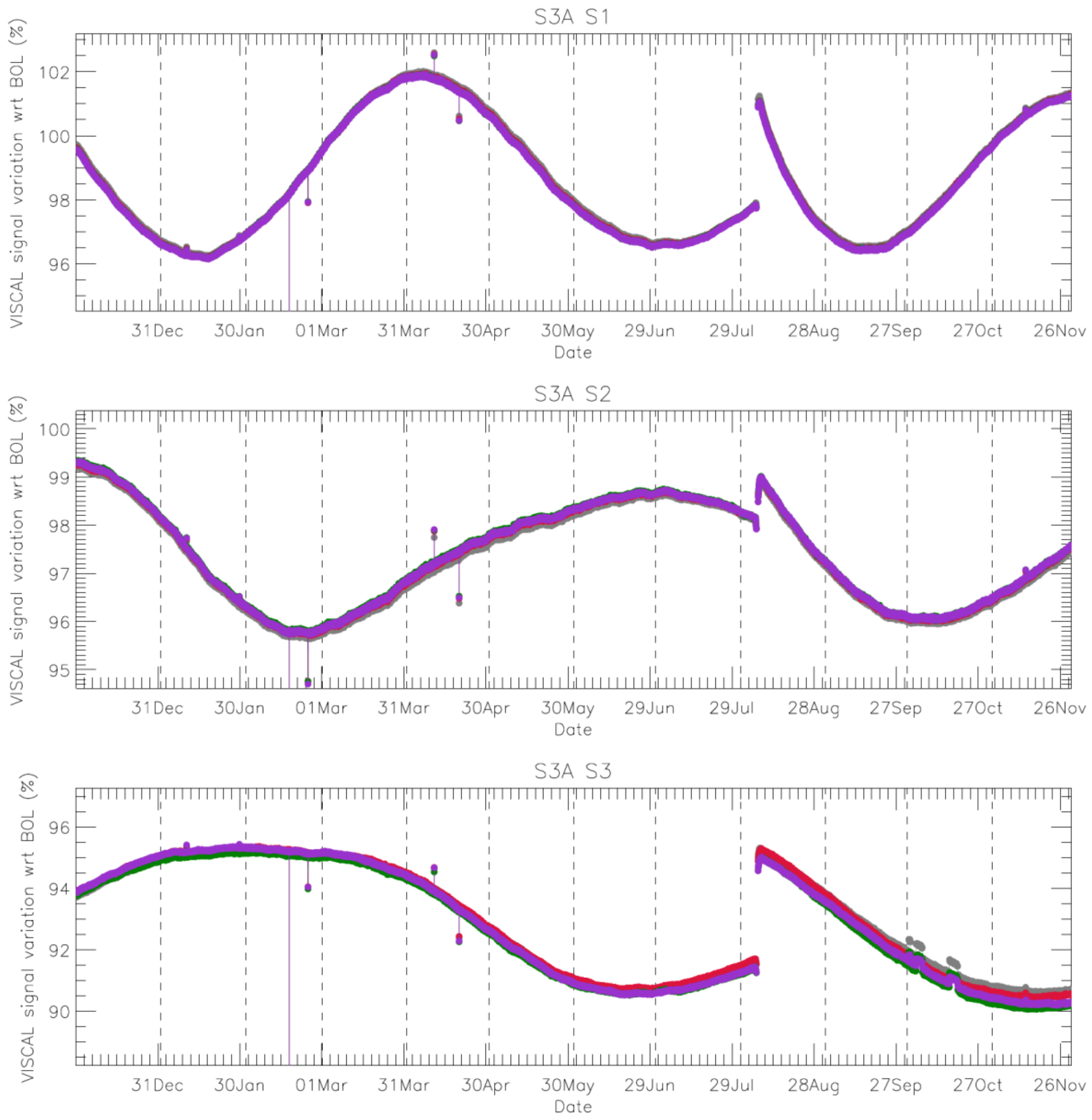

*Figure 16: Variation of the radiometric gain derived from the VISCAL signals for SLSTR-A VIS channels for the last year of operations (nadir view). Different colours represent different detectors. The vertical dashed lines indicate the start of each month.*

**SWIR VISCAL signal variation over the past year**

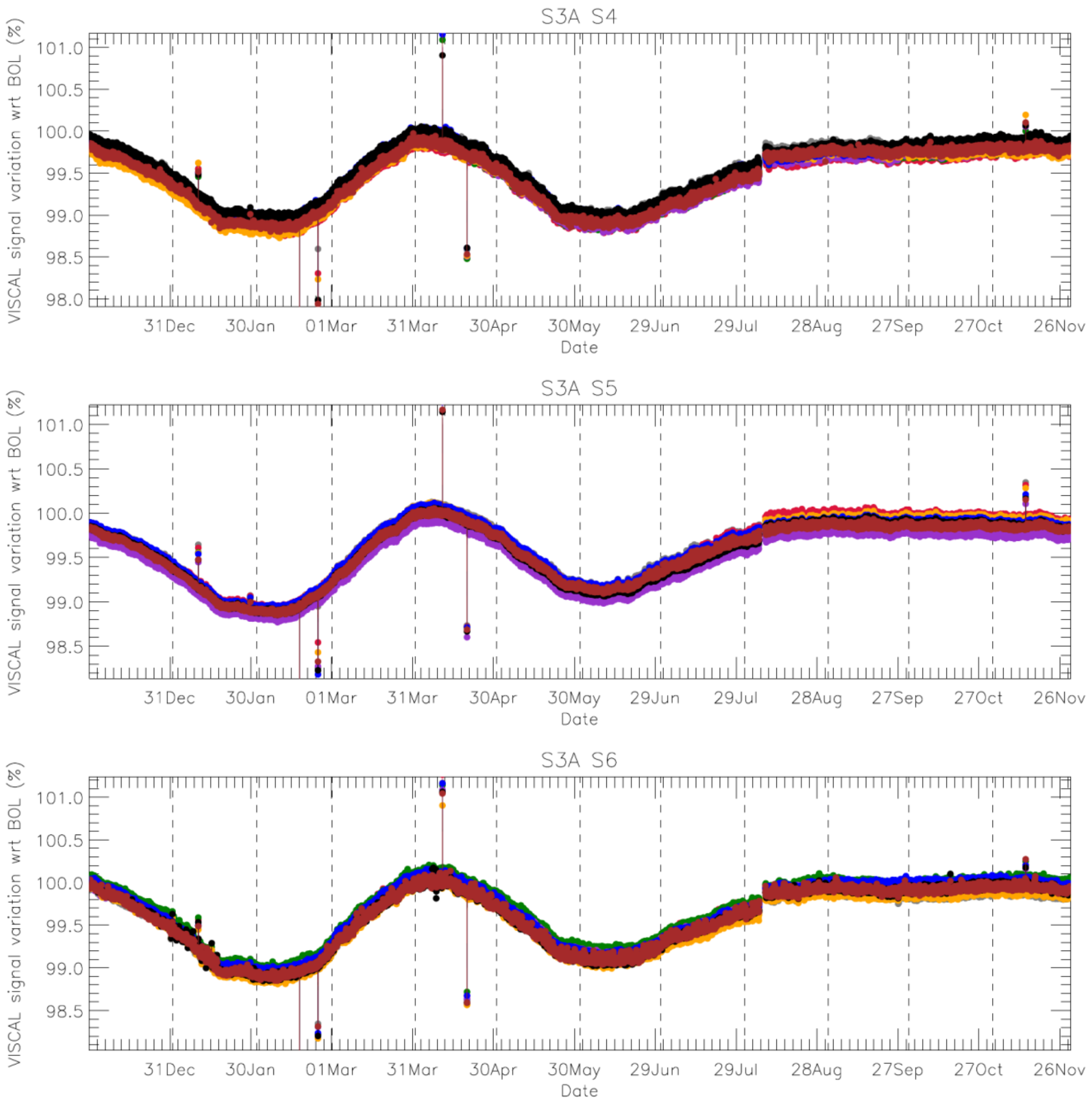

***Figure 17: Variation of the radiometric gain derived from the VISCAL signals for SLSTR-A SWIR channels for the last year of operations (nadir view). Different colours represent different detectors. The vertical dashed lines indicate the start of each month.***

### 4.6.3 SLSTR-B

Figure 18 and Figure 19 show the variation of the radiometric gain derived from the VISCAL signals for SLSTR-B over the past year. The data from the last month appears normal and follows the expected trend. There are several features in this annual trend plot to note.

- There is noisy behaviour and numerous drops in signal in the radiometric gain, especially in channels S1 and S2. This gives 2-3% errors in the radiometric calibration of these channels. A number of candidate root causes have been identified, with the most likely due to motional chopping of the VIS detectors by an internal aperture in the VIS optical bench. Because the effect appears to be random it is most likely affecting all the data for S1 and S2.

**VIS VISCAL signal variation over the past year**

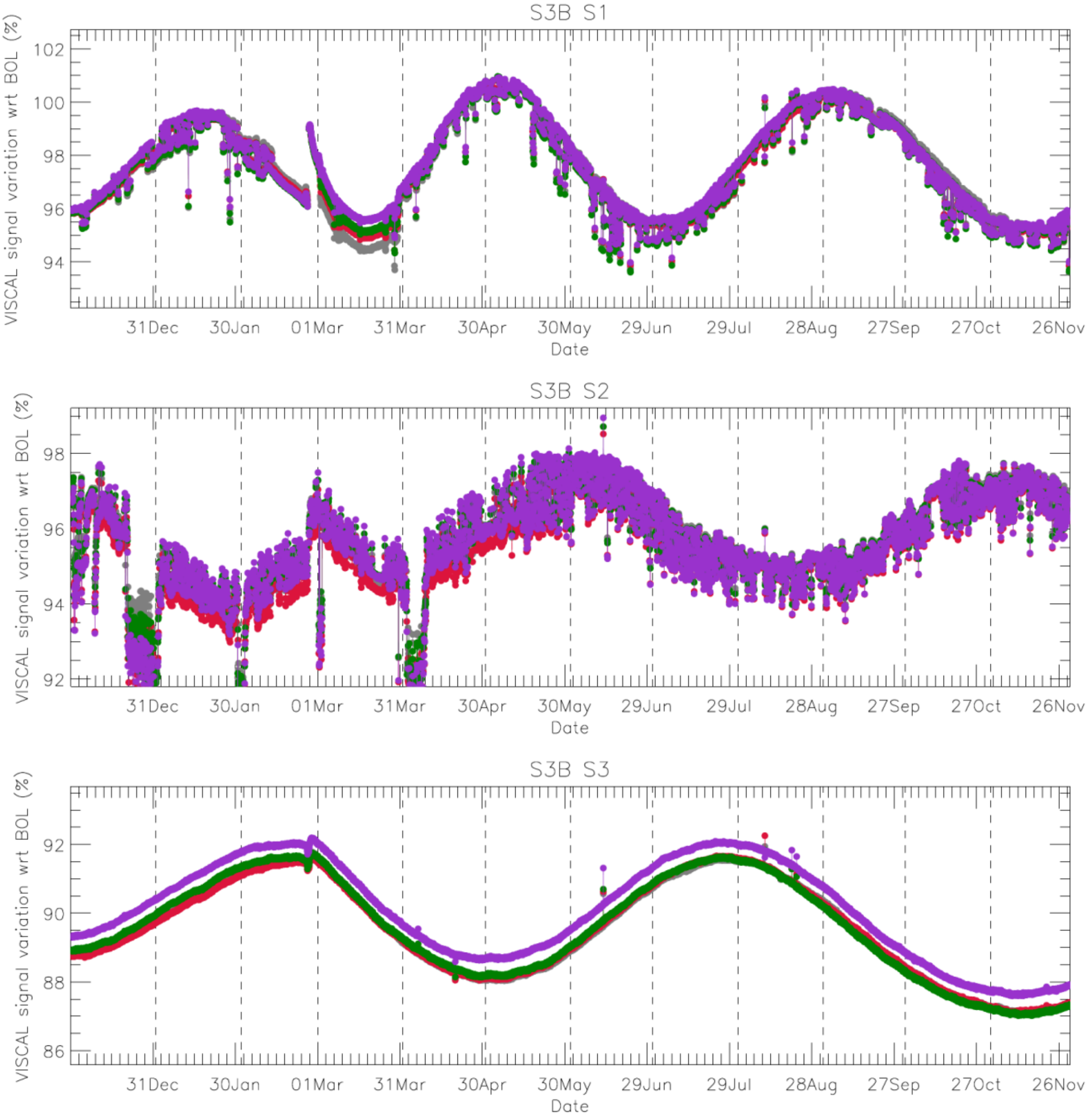

*Figure 18: Variation of the radiometric gain derived from the VISCAL signals for SLSTR-B VIS channels for the past year (nadir view). Different colours represent different detectors. The vertical dashed lines indicate the start of each month.*

## SWIR VISCAL signal variation over the past year

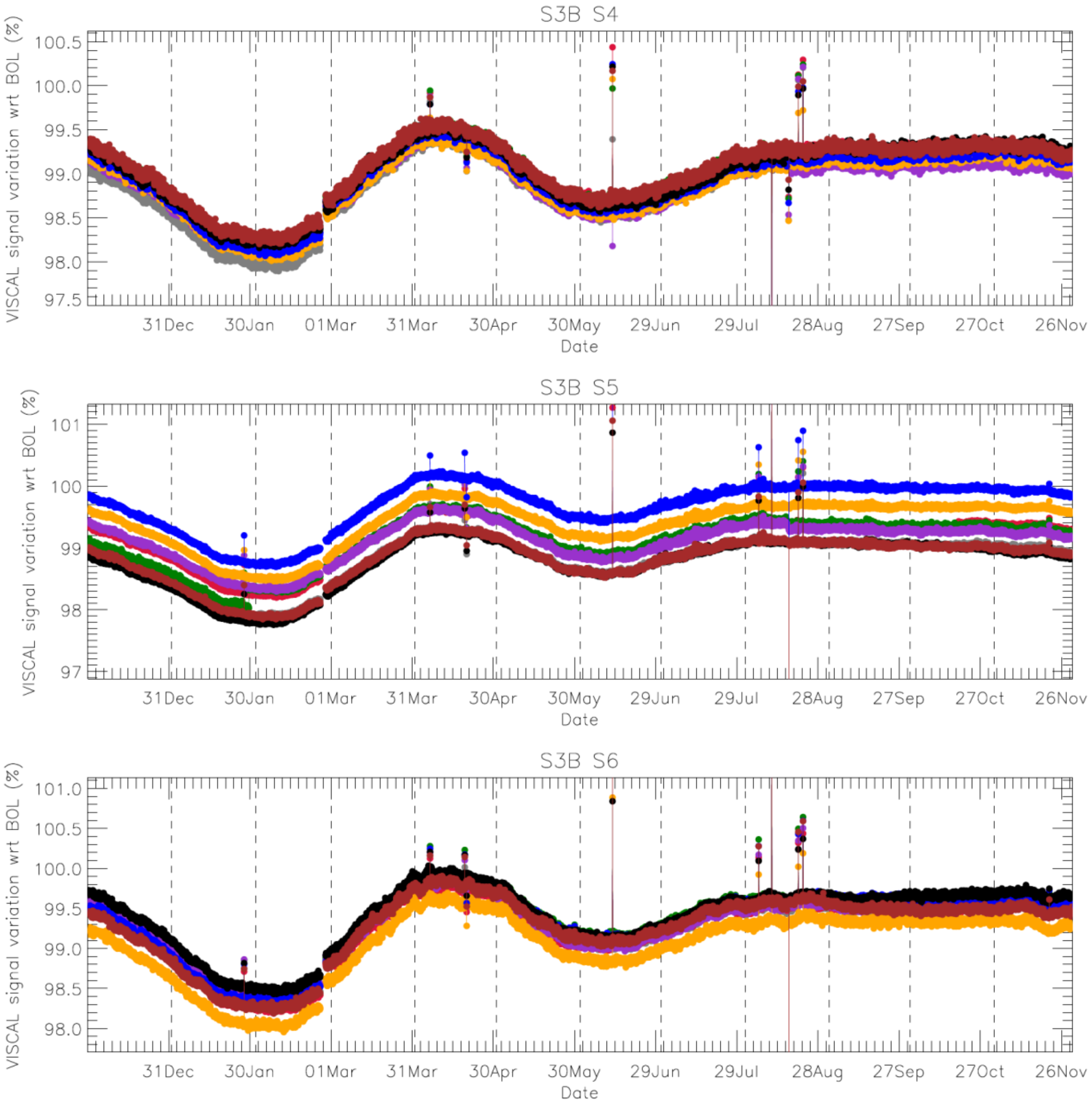

*Figure 19: Variation of the radiometric gain derived from the VISCAL signals for SLSTR-B SWIR channels for the past year (nadir view). Different colours represent different detectors. The vertical dashed lines indicate the start of each month.*

# 5 Level-1 product validation

**Level-1 product quality is assessed in terms of radiometric and geometric accuracy**

The Level-1 image quality is assessed when data are available at the MPC. For example, by combining all granules over one day into a single combined image. The S3A and S3B satellites are configured to be 140 degrees out of phase in order to observe complimentary portions of the earth. Figure 20 shows an example combined SLSTR-A/SLSTR-B image for the visible channels on 29th of November 2023 (daytime only).

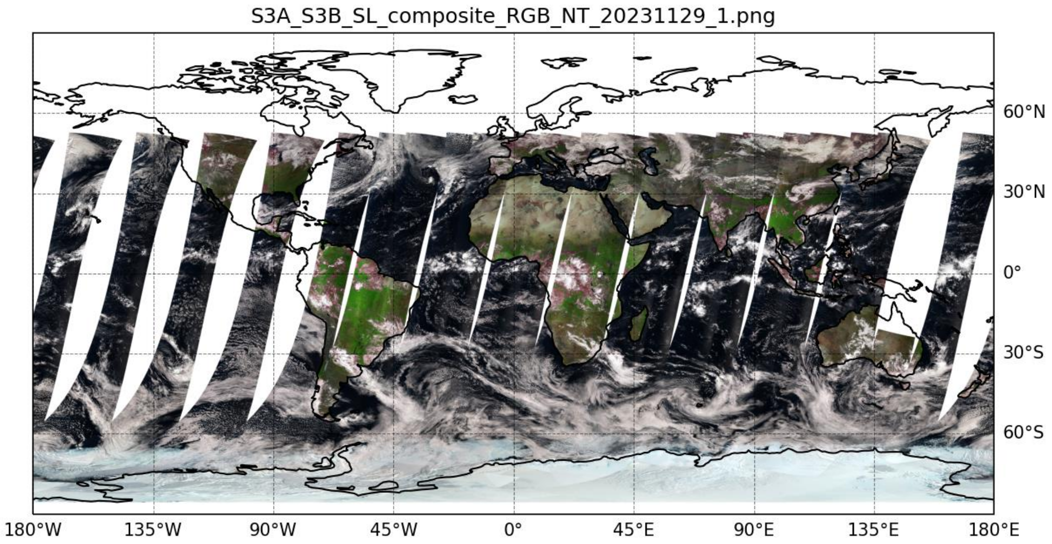

***Figure 20: Daytime combined SLSTR-A and SLSTR-B Level-1 image for visible channels on 29th of November 2023.***

## 5.1 Level-1 TIR Radiometric Validation

**S3_MR_1000 Relative radiometric accuracy:** Sentinel-3 infrared channels shall have a relative radiometric accuracy of <0.08K (threshold) with a goal of 0.05 K over a range of 210-350 K expressed as NEDT traceable to international reference standards.

The absolute radiometric calibration of the IR channels is being validated by EUMETSAT using comparisons against IASI-A and B (Tomazic et al 2018). These results confirmed very good performance with almost no bias (< 0.1 K) for channels S8 and S9 in the nadir view over the temperature range 220 – 280 K.

## 5.2 Level- 1 VIS SWIR Radiometric Validation

**A3_MR_1010 Absolution radiometric accuracy:** Sentinel-3 VIS reflectance at TO shall have an absolute radiometric accuracy goal of < 2% with reference to the sun for the 400-900 nm wavebands and <5% with reference to the sun for wavebands >900 nm traceable to international reference standards.

Validation of the VIS/SWIR radiometric measurements is performed by various methods to establish the magnitude of any calibration offset. Some activities are routinely performed each month and reported here, and some are less regular and reported in the annual data quality reports.

The results of these different methods have been collated and have been found to agree that there is a calibration offset present in the VIS/SWIR radiances. It is recommended therefore that users apply an offset in-line with the values presented in Table 7. These offsets are stable and apply to the entire mission. Note that uncertainty estimates are at k=1.

| **Nadir View** | **S1** | **S2** | **S3** | **S5** | **S6** |
|---|---|---|---|---|---|
| Correction | 0.97 | 0.98 | 0.98 | 1.11 | 1.13 |
| Uncertainty | 0.03 | 0.02 | 0.02 | 0.02 | 0.02 |
| **Oblique View** | **S1** | **S2** | **S3** | **S5** | **S6** |
| Correction | 0.94 | 0.95 | 0.95 | 1.04 | 1.07 |
| Uncertainty | 0.05 | 0.03 | 0.03 | 0.03 | 0.05 |

***Table 7. The recommended corrections that should be applied to SLSTR-A and SLSTR-B VIS, SWIR channels.***

### 5.2.1 Radiometric validation with DIMITRI

#### 5.2.1.1 Verification and Validation over PICS

1. The ingestion of the available L1-RBT-NT products from SLSTR-A and SLSTR-B over the 6 desert CalVal-sites (Algeria3 & 5, Libya 1 & 4 and Mauritania 1 & 2) has been performed until the **end-November 2023**.
2. The results are consistent over all the six used PICS sites (Figure 21 and Figure 22). Both sensors show a good stability over the analysed period over VNIR bands for both NADIR & OBLIQUE views, with slight positive trend.
3. The temporal average over the period **1$^{st}$ January 2023 - end-November 2023** of the elementary ratios (observed reflectance to the simulated one) for **SLSTR-A** and **SLSTR-B** show gain values between 3-6% (NADIR) and 6-9% (OBLIQUE) over the VNIR bands S1-S3 (Figure 23).

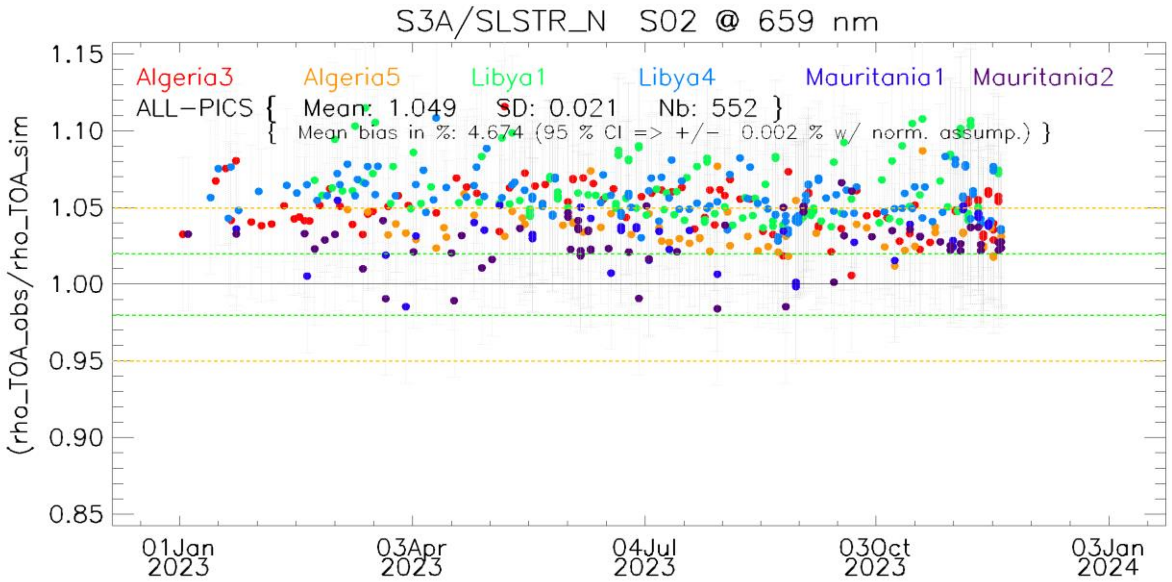
S3A/SLSTR_N S02 @ 659 nm
Algeria3
Algeria5
Libya1
Libya4
Mauritania1
Mauritania2
ALL–PICS { Mean: 1.049 SD: 0.021 Nb: 552 }
{ Mean bias in %: 4.674 (95 % CI => +/– 0.002 % w/ norm. assump.) }
(rho_TOA_obs/rho_TOA_sim
1.15
1.10
1.05
1.00
0.95
0.90
0.85
01Jan 2023
03Apr 2023
04Jul 2023
03Oct 2023
03Jan 2024

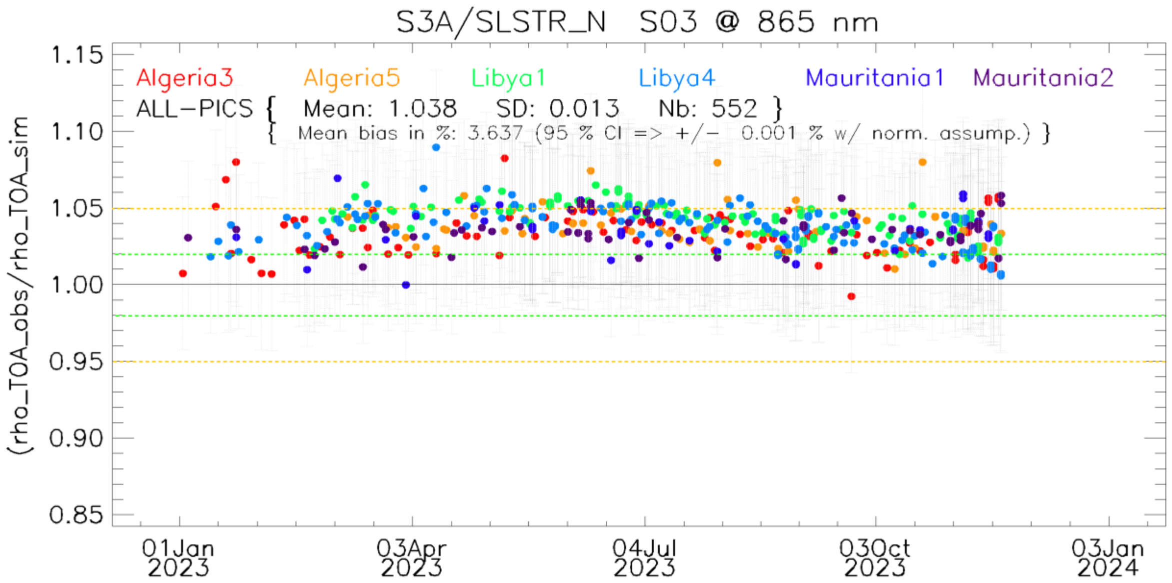
S3A/SLSTR_N S03 @ 865 nm
Algeria3
Algeria5
Libya1
Libya4
Mauritania1
Mauritania2
ALL–PICS { Mean: 1.038 SD: 0.013 Nb: 552 }
{ Mean bias in %: 3.637 (95 % CI => +/– 0.001 % w/ norm. assump.) }
(rho_TOA_obs/rho_TOA_sim
1.15
1.10
1.05
1.00
0.95
0.90
0.85
01Jan 2023
03Apr 2023
04Jul 2023
03Oct 2023
03Jan 2024

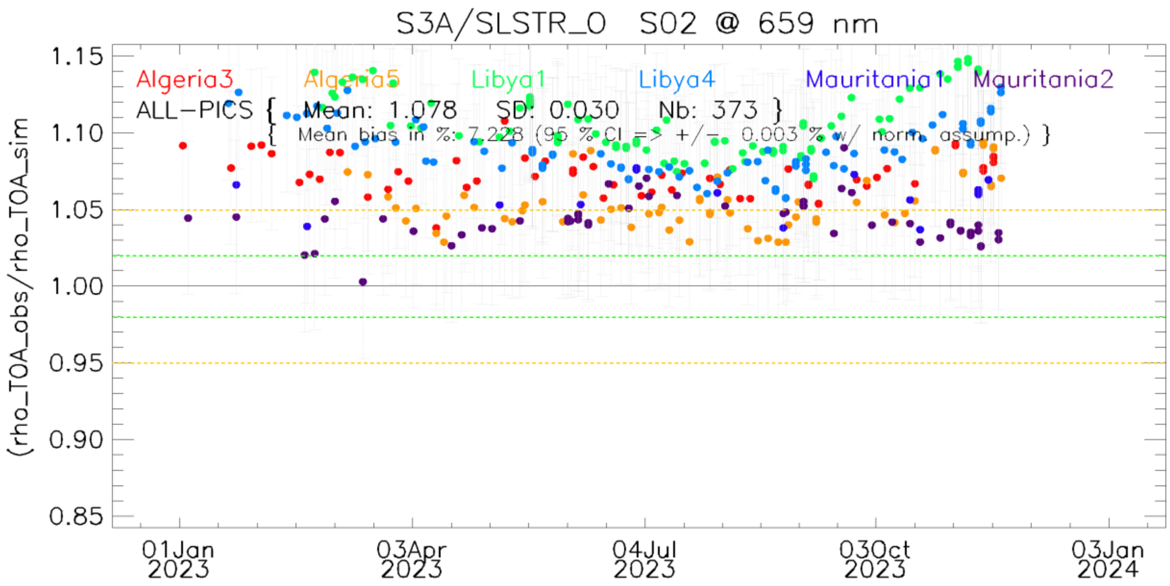

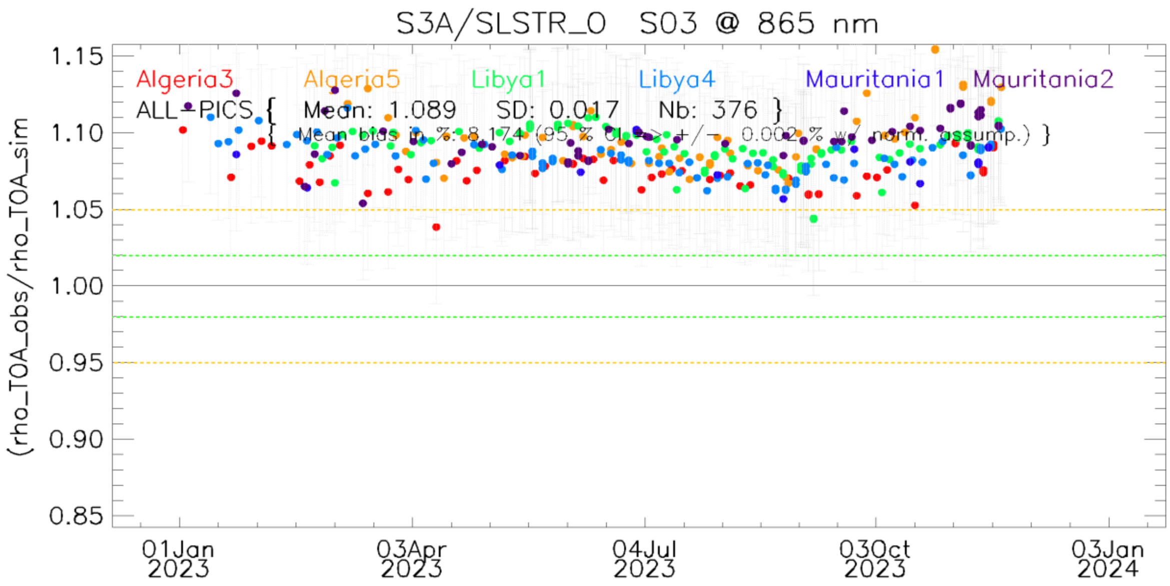

*Figure 21: Time-series of the elementary ratios (observed/simulated) signal from SLSTR-A for (top to bottom) bands S02 and S03 (Nadir & Oblique views) respectively over January 2023- November 2023 from the six PICS Cal/Val sites. Dashed-green and orange lines indicate the 2% and 5% respectively. Error bars indicate the desert methodology uncertainty.*

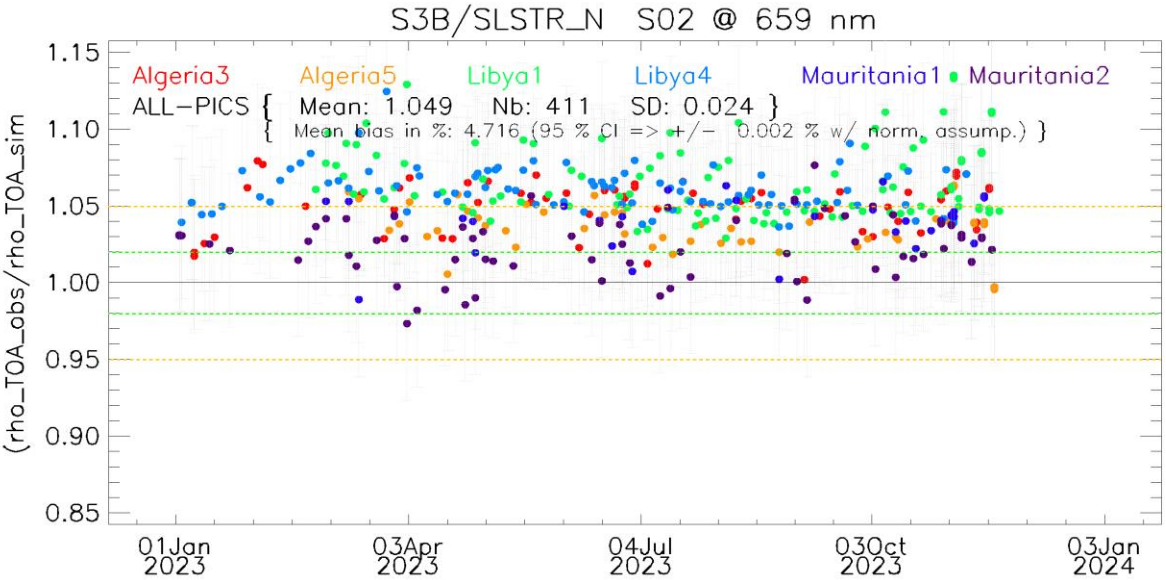
S3B/SLSTR_N S02 @ 659 nm
Algeria3
Algeria5
Libya1
Libya4
Mauritania1
Mauritania2
ALL–PICS { Mean: 1.049 Nb: 411 SD: 0.024 }
{ Mean bias in %: 4.716 (95 % CI => +/– 0.002 % w/ norm. assump.) }
(rho_TOA_obs/rho_TOA_sim
1.15
1.10
1.05
1.00
0.95
0.90
0.85
01Jan 2023
03Apr 2023
04Jul 2023
03Oct 2023
03Jan 2024

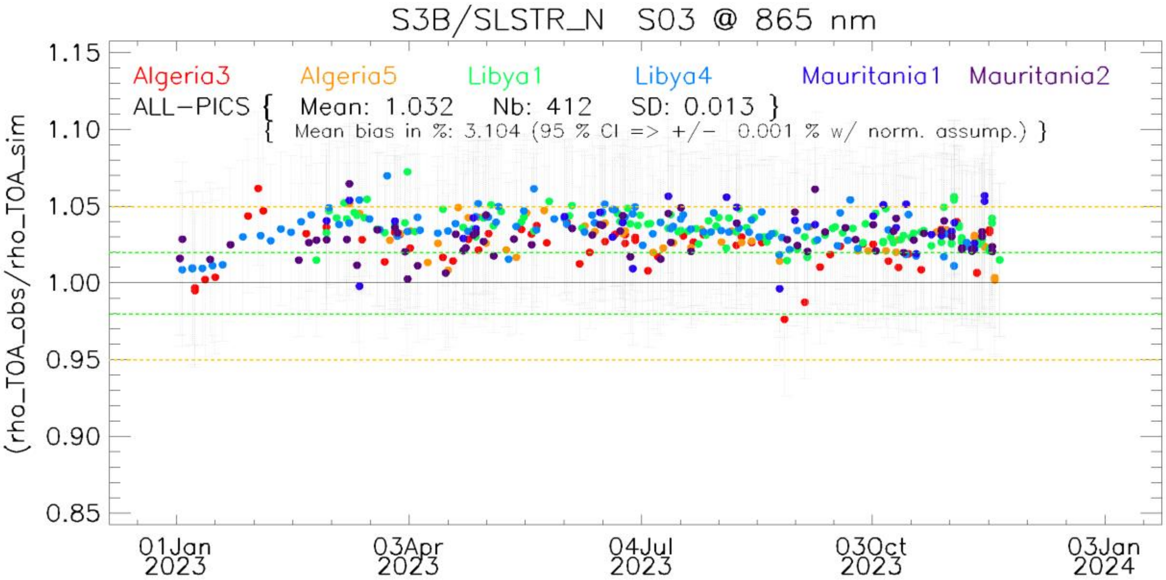
S3B/SLSTR_N S03 @ 865 nm
Algeria3
Algeria5
Libya1
Libya4
Mauritania1
Mauritania2
ALL–PICS { Mean: 1.032 Nb: 412 SD: 0.013 }
{ Mean bias in %: 3.104 (95 % CI => +/– 0.001 % w/ norm. assump.) }
(rho_TOA_obs/rho_TOA_sim
1.15
1.10
1.05
1.00
0.95
0.90
0.85
01Jan 2023
03Apr 2023
04Jul 2023
03Oct 2023
03Jan 2024

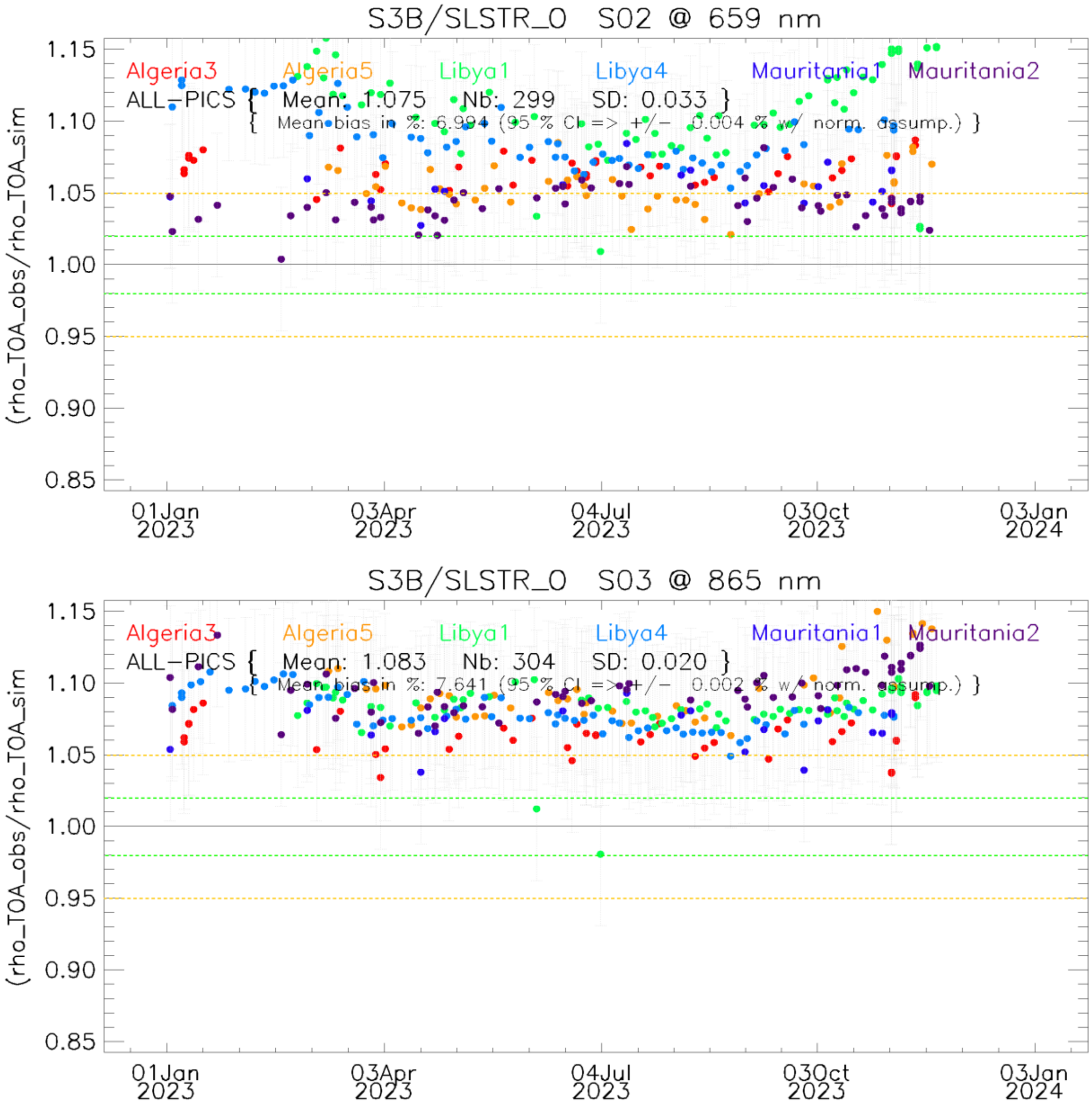

*Figure 22: Time-series of the elementary ratios (observed/simulated) signal from SLSTR-B for (top to bottom) bands S02 and S03 (Nadir & Oblique views) respectively over January 2023- end-November 2023 from the six PICS Cal/Val sites. Dashed-green and orange lines indicate the 2% and 5% respectively. Error bars indicate the desert methodology uncertainty.*

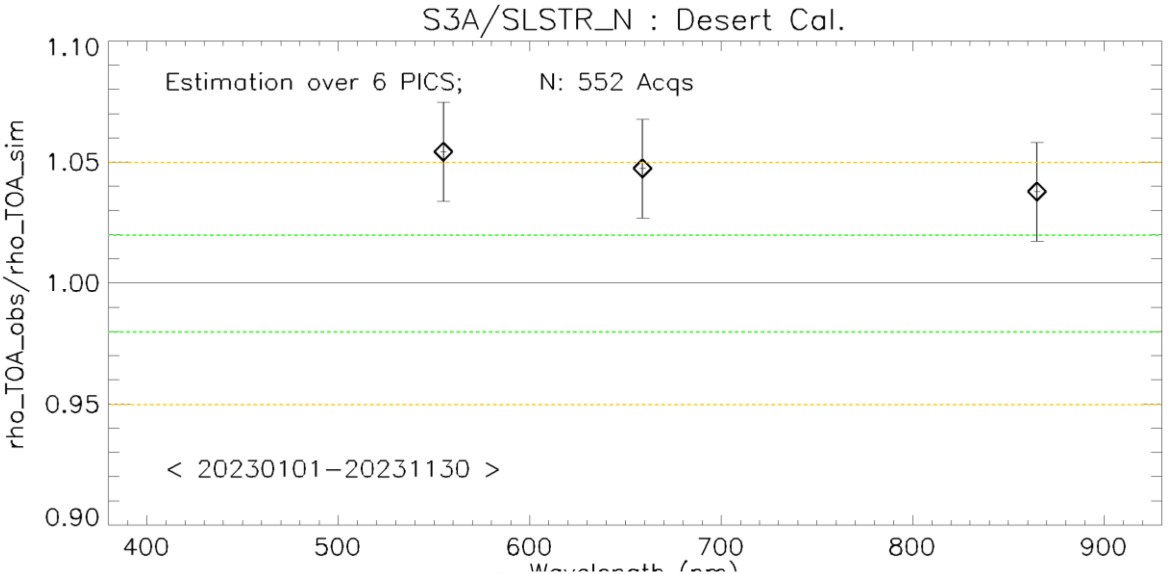
S3A/SLSTR_N : Desert Cal.
Estimation over 6 PICS;
N: 552 Acqs
< 20230101–20231130 >
rho_TOA_obs/rho_TOA_sim
1.10
1.05
1.00
0.95
0.90
400
500
600
700
800
900

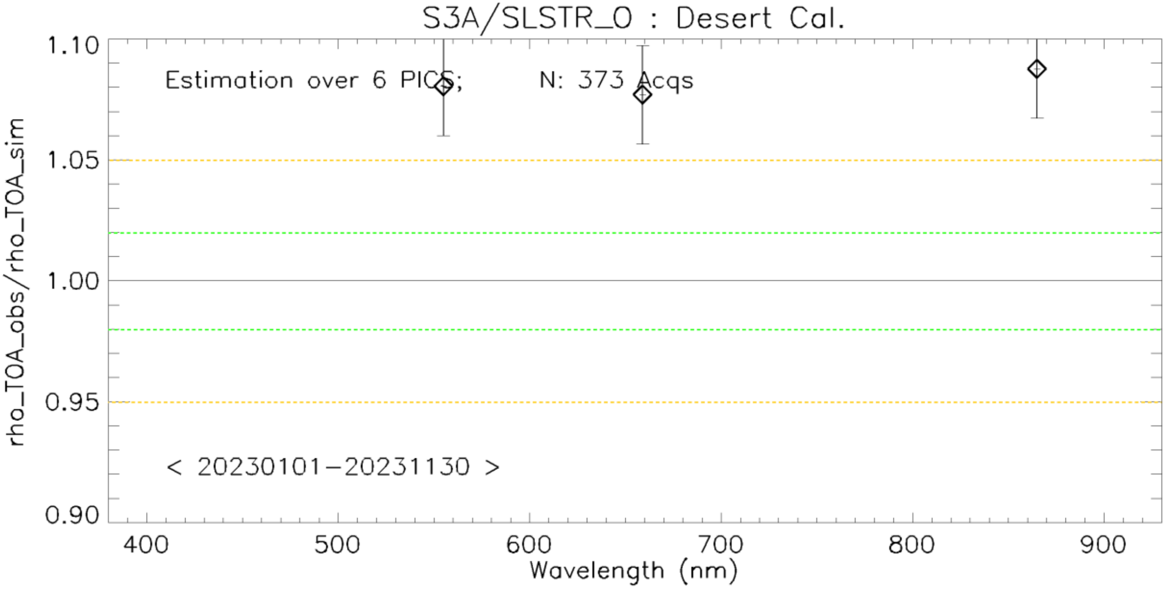
S3A/SLSTR_O : Desert Cal.
Estimation over 6 PICS;
N: 373 Acqs
< 20230101–20231130 >
rho_TOA_obs/rho_TOA_sim
1.10
1.05
1.00
0.95
0.90
400
500
600
700
800
900
Wavelength (nm)

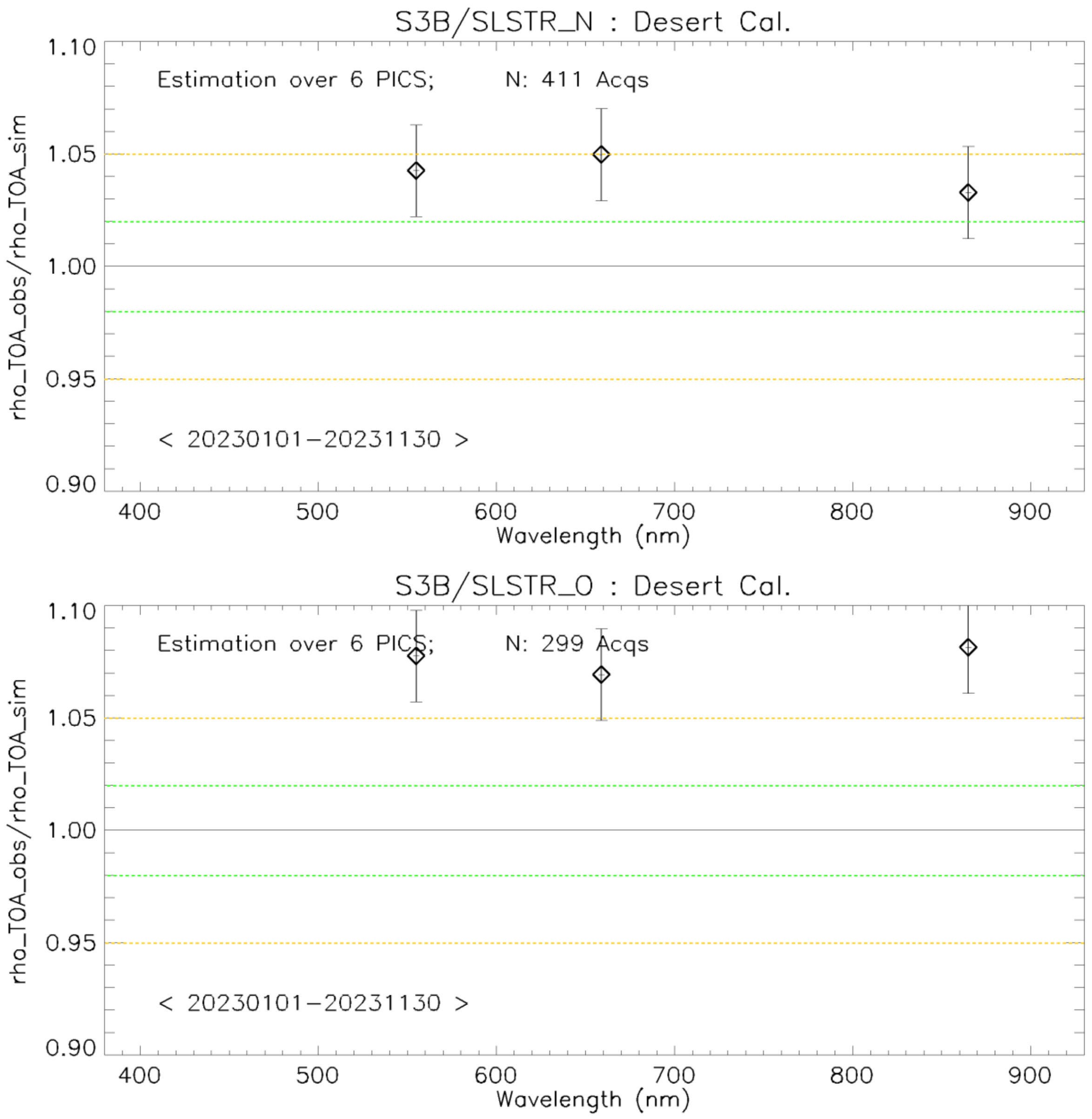

***Figure 23: The estimated gain values for SLSTR-A and SLSTR-B (top to bottom) Nadir & Oblique views respectively over the 6 PICS sites identified by CEOS over the period January 2023- end-November 2023 as a function of wavelength. Dashed-green and orange lines indicate the 2% and 5% respectively. Error bars indicate the desert methodology uncertainty.***

#### 5.2.1.2 Validation over Rayleigh

Rayleigh method has been performed from the available mini-files over the period **January 2022- end-November 2023** for SLSTR-A and SLSTR-B. The gain coefficients of both sensors are consistent with the previous results (Figure 24).

### 5.2.1.3 Validation over Glint

Glint calibration method has been performed over the period **January 2022- end-November 2023** for both SLSTR-A and SLSTR-B. The gain coefficients of both sensors are consistent with the previous results over the Nadir view (Figure 24).

### 5.2.1.4 Validation results synthesis

The results synthesis displayed below on Figure 24.

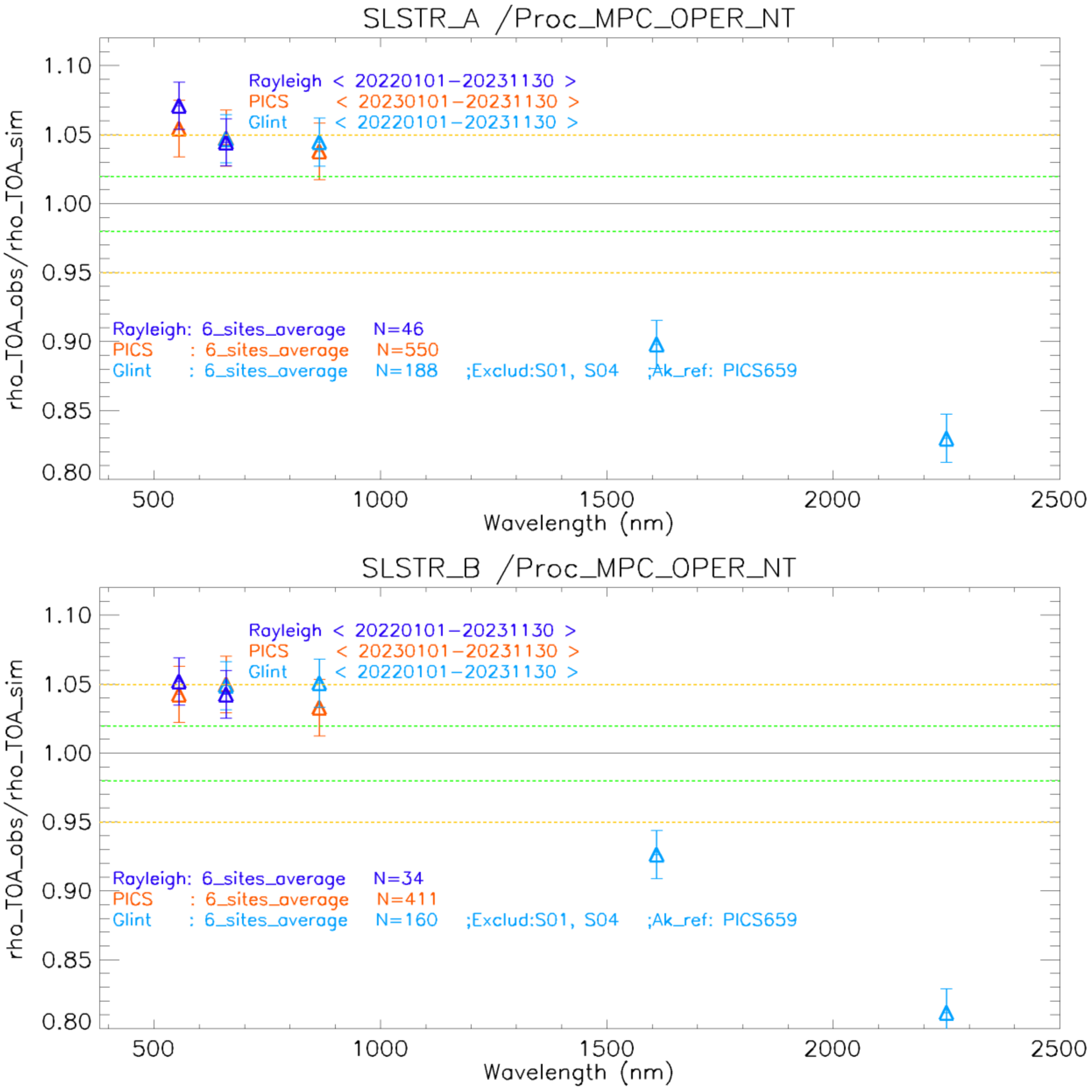

*Figure 24: The estimated gain values for SLSTR-A and SLSTR-B (Nadir view) from Glint and Rayleigh methods over the period Jan 2022—end-November 2023 and PICS method over the period Jan 2023—end-November 2023 as a function of wavelength. We use the gain value of S02 from Desert-PICS method as reference gain for Glint method. Dashed-green and orange lines indicate the 2% and 5% respectively. Error bars indicate the method uncertainties*

#### 5.2.1.5 Cross-mission Intercomparison over PICS:

X-mission Intercomparison between SLSTR-A, SLSTR-B, MERIS, MSI-A, MSI-B, OLCI-A and OLCI-B has been performed over the 6 PICS-test-sites. Figure 25 shows the estimated gain over different time-series for different sensors over PICS. The spectral bands with significant absorption of water vapor and O2 are excluded. OLCI-A, SLSTR-A and SLSTR-B seem to have higher gain wrt the other sensors of about 1-4% over VNIR spectral range.

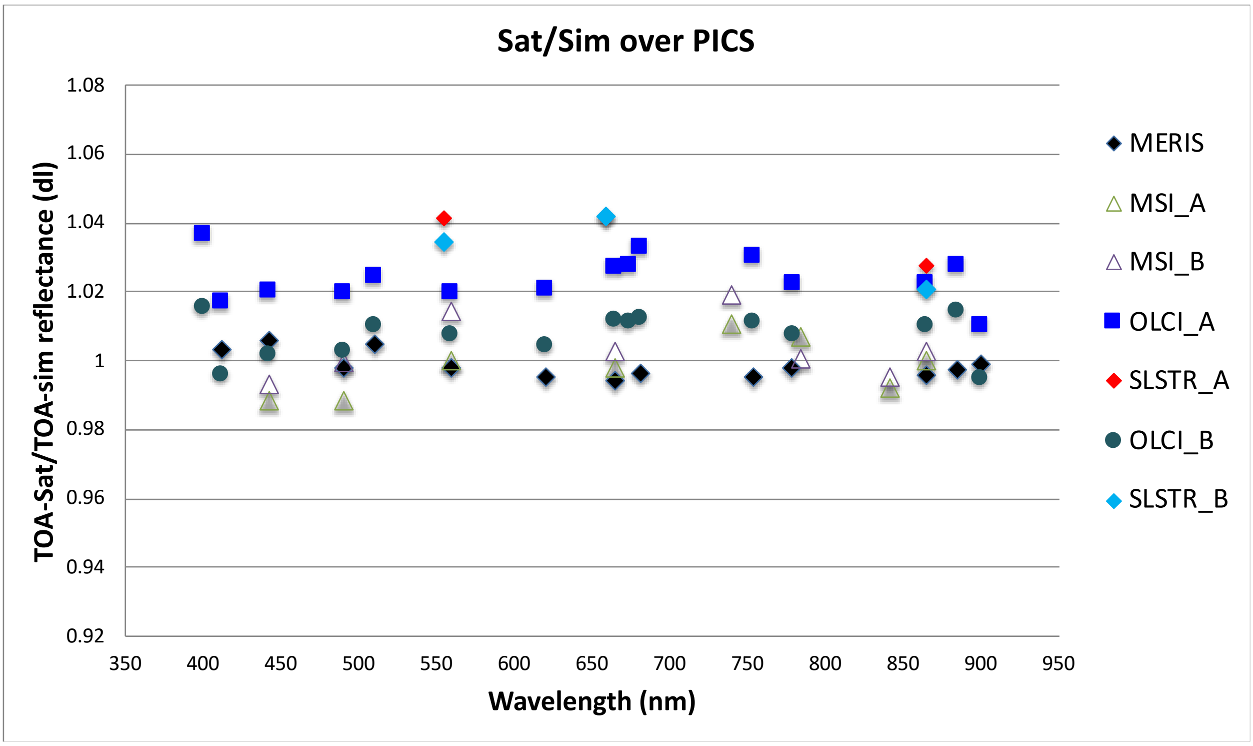

*Figure 25: Ratio of observed TOA reflectance to simulated one for (black) MERIS, (pale-green) S2A/MSI, (white) S2B/MSI, (blue) S3A/OLCI, (green) S3B/OLCI, (red) S3A/SLSTR-NADIR, and (cyan) S3B/SLSTR-NADIR averaged over the six PICS test sites as a function of wavelength.*

## 5.3 Level-1 Geometric Validation

**S3_MR_1090 Geolocation accuracy:** Improved geo-location accuracy is possible when using ground control points and Sentinel-3 shall be designed to ensure a geolocation accuracy of better than 0.5rm of the spatial resolution of the optical sensor when using ground control points.

**S3_MR_1100 Inter channel co-registration.** The inter channel spatial co-registration for Sentinel-3 visible measurements shall be < 0.5 of the spatial resolution of the sensor over the full spectral range (goal of 0.3 of the spatial resolution of the sensor)

**S3_MR_1100 Inter channel co-registration:** The inter channel spatial co-registration for Sentinel-3 SWIR and TIR measurements shall be sufficient to allow these channels to be co registered with visible channels at higher spatial resolution data.

Regular monitoring using the GeoCal Tool implemented at the MPC is normally carried out. On average, the geolocation accuracy of the VIS-SWIR channels meets requirements for SLSTR-A and SLSTR-B.

GeoCal is a tool that monitors the geolocation performance in Level-1 images by correlation of the images with reference features containing ground control points (GCP). Each Level-1 granule typically contains several hundred GCPs if over land, which are filtered based on signal-to-noise to obtain a daily average in the across and along track directions.

The geolocation uncertainty is stable and within requirements during the reporting period.

### 5.3.1 SLSTR-A

The results for November 2023 are plotted in Figure 26 for SLSTR-A, giving the average positional offsets in kilometres for Nadir and Oblique views.

**GEOCAL Offsets over the last month**

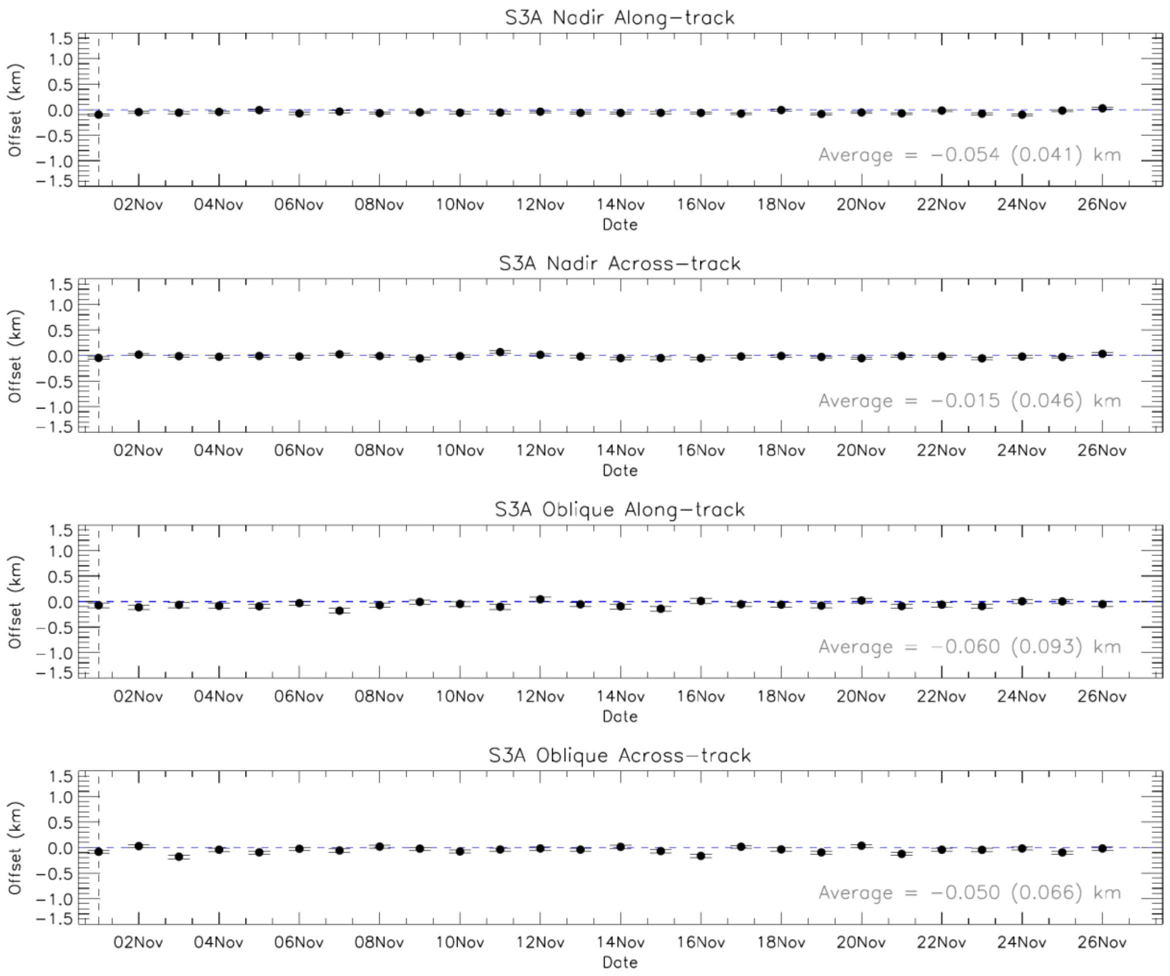

*Figure 26: SLSTR-A daily offset results in km from the GeoCal Tool analysis for Nadir along- and across-track (top two plots) and Oblique along- and across-track (bottom two plots) for November 2023. The error bars show the standard deviation.*

### 5.3.2 SLSTR-B

The results for November 2023 are plotted in Figure 27 for SLSTR-B, giving the average positional offsets in kilometres for Nadir and Oblique views.

**GEOCAL Offsets over the last month**

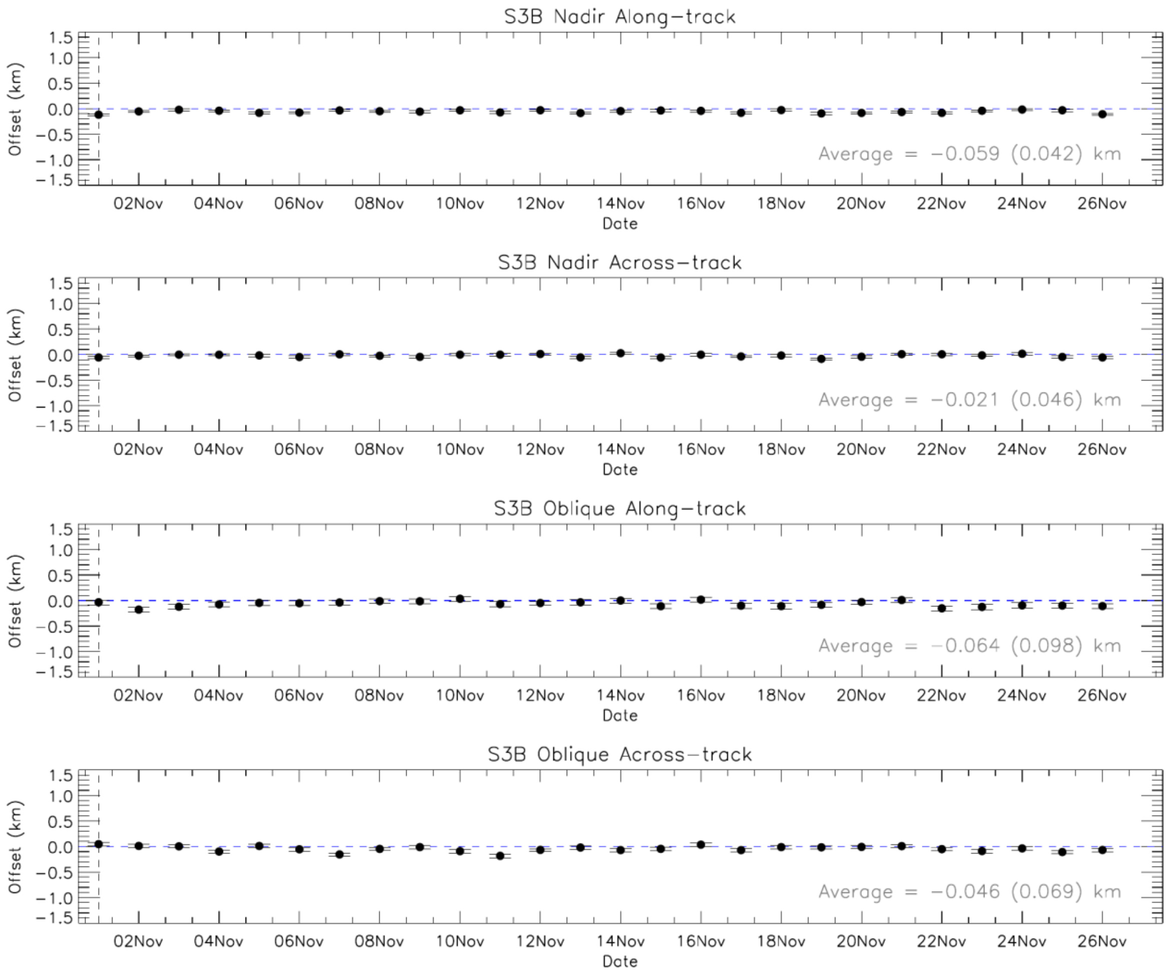

*Figure 27: SLSTR-B daily offset results in km from the GeoCal Tool analysis for Nadir along- and across-track (top two plots) and Oblique along- and across-track (bottom two plots) for November 2023. The error bars show the standard deviation.*

# 6 Level 2 LST validation

Level 2 Land Surface Temperature products have been validated against *in situ* observations (Category-A validation) from eight "Gold Standard" Stations. The different categories of validation are first described in the LST Validation Protocol (Schneider et al., 2012) and reinforced in the CEOS WGCV-LPV Land Surface Temperature Product Validation Best Practice Protocol (Guillevic et al., 2017). In all cases it is the NTC products that are validated, and the Probabilistic cloud masking implementation is used for all cloud masking. Both S3A and S3B L2 products are produced with the updated LST coefficients following the operational release on 25th February 2019. In each case the latest temporal interpolation for the probabilistic cloud mask is applied following the L1 operational release on 15th January 2020. The updated cloud coefficients ADF was applied on 23rd October 2020.

## 6.1 Category-A validation

Category-A validation uses a comparison of satellite-retrieved LST with *in situ* measurements collected from radiometers sited at a number of stations spread across the Earth, for which the highest-quality validation can be achieved. Here we concentrate on twelve "Gold Standard" stations which are installed with well-calibrated instrumentation: twelve from the SURFRAD network (Bondville, Illinois; Desert Rock, Nevada; Fort Peck, Montana; Goodwin Creek, Mississippi; Penn State University, Pennsylvania; Sioux Fall, South Dakota; Table Mountain, Colorado); two from the ARM network (Southern Great Plains, Oklahoma; Barrow, Alaska); and three from the USCRN network (Williams, Arizona; Des Moines, Iowa; Manhatten, Kansas).

For the SURFRAD field pyrgeometers the uncertainty is estimated to be ±5 Wm-2 (Augustine and Dutton, 2013). For ARM, the uncertainty of the measured brightness temperatures was set to ±0.5 K for Southern Great Plains (Morris, 2006), and for North Slopes Alaska the uncertainty of the IR radiance data was set to ±4 Wm-2 (Stoffel, 2006). For the USCRN network, which uses Apogee SI-121s the uncertainty is set as the manufacturers estimate of ±0.2 K.

The results can be summarised as follows (accuracy is used as the metric rather than uncertainty as this is then a straight comparison with mission requirements):

***Table 8: Average absolute accuracy in K of the SL_2_LST product with respect to Gold Standard stations for Q3 2023.***

| Satellite | Day | Night |
|---|---|---|
| S3A | 1.5 | 1.2 |
| S3B | 1.7 | 1.2 |

For both SLSTR-A and SLSTR-B both the daytime and night-time absolute accuracies (which are derived from the absolute values of all the mean biases from the individual stations) are greater than the mission requirement of 1K, but driven by larger biases at some sites. The main impact on accuracy and precision is driven by any errors in the cloud masking, but also higher temperatures. The recommendation would be to assess whether an improvement could be made with the retrieval coefficients particularly during the day for higher temperatures.

| SLSTR-A | SLSTR-B |
|---|---|
| 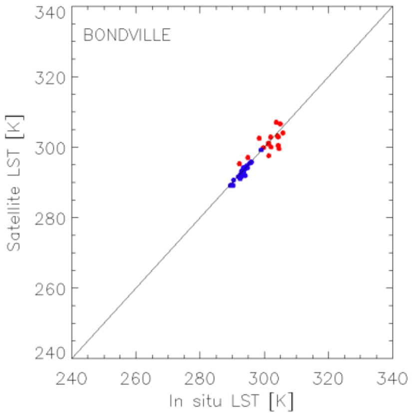 | 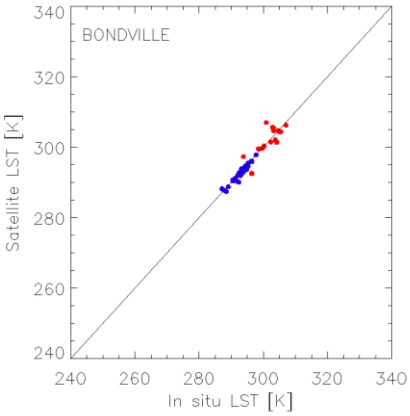 |
| 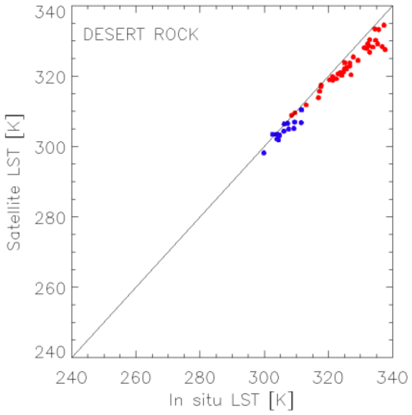 | 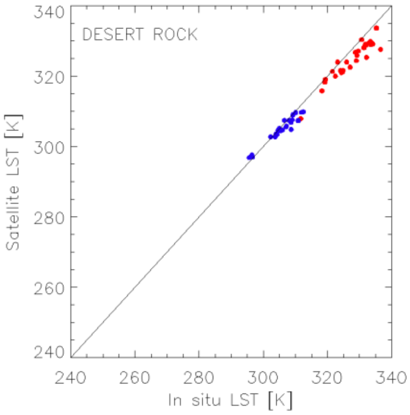 |
| 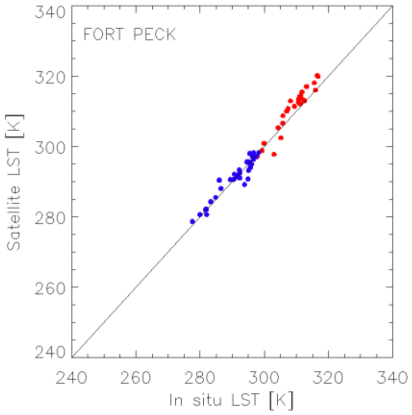 | 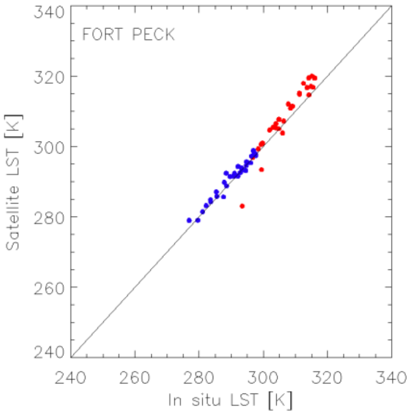 |

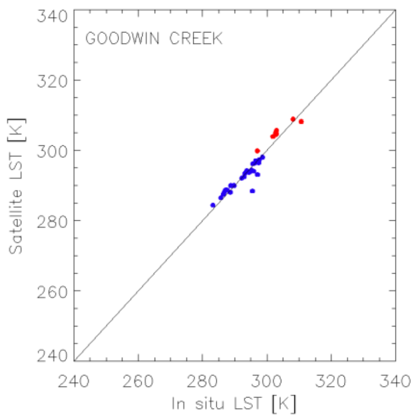
GOODWIN CREEK
Satellite LST [K]
In situ LST [K]
240
260
280
300
320
340

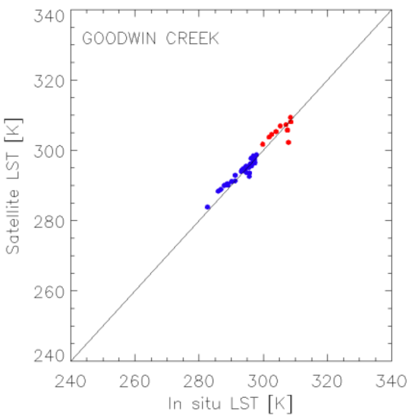
GOODWIN CREEK
Satellite LST [K]
In situ LST [K]
240
260
280
300
320
340

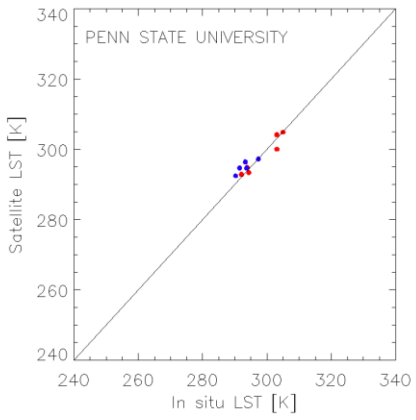
PENN STATE UNIVERSITY
Satellite LST [K]
In situ LST [K]
240
260
280
300
320
340

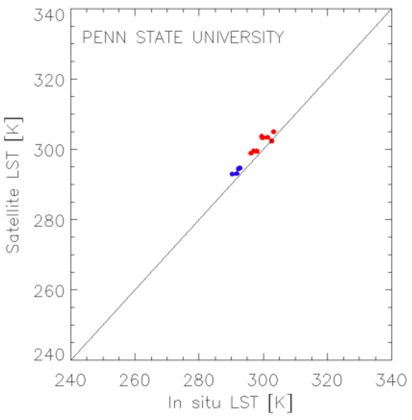
PENN STATE UNIVERSITY
Satellite LST [K]
In situ LST [K]
240
260
280
300
320
340

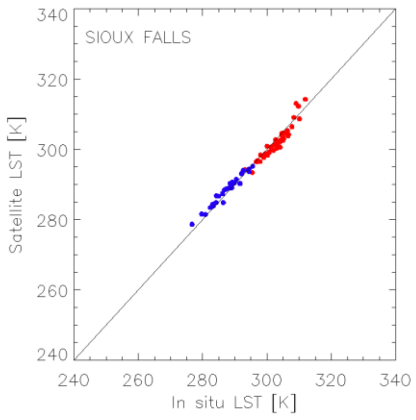
SIOUX FALLS
Satellite LST [K]
In situ LST [K]
240
260
280
300
320
340

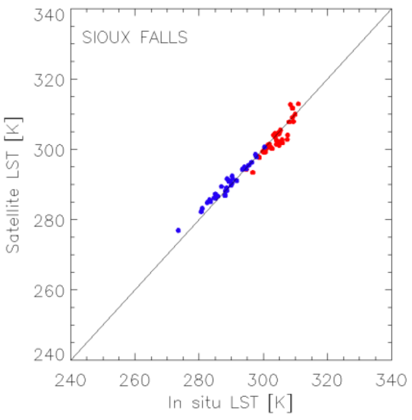
SIOUX FALLS
Satellite LST [K]
In situ LST [K]
240
260
280
300
320
340

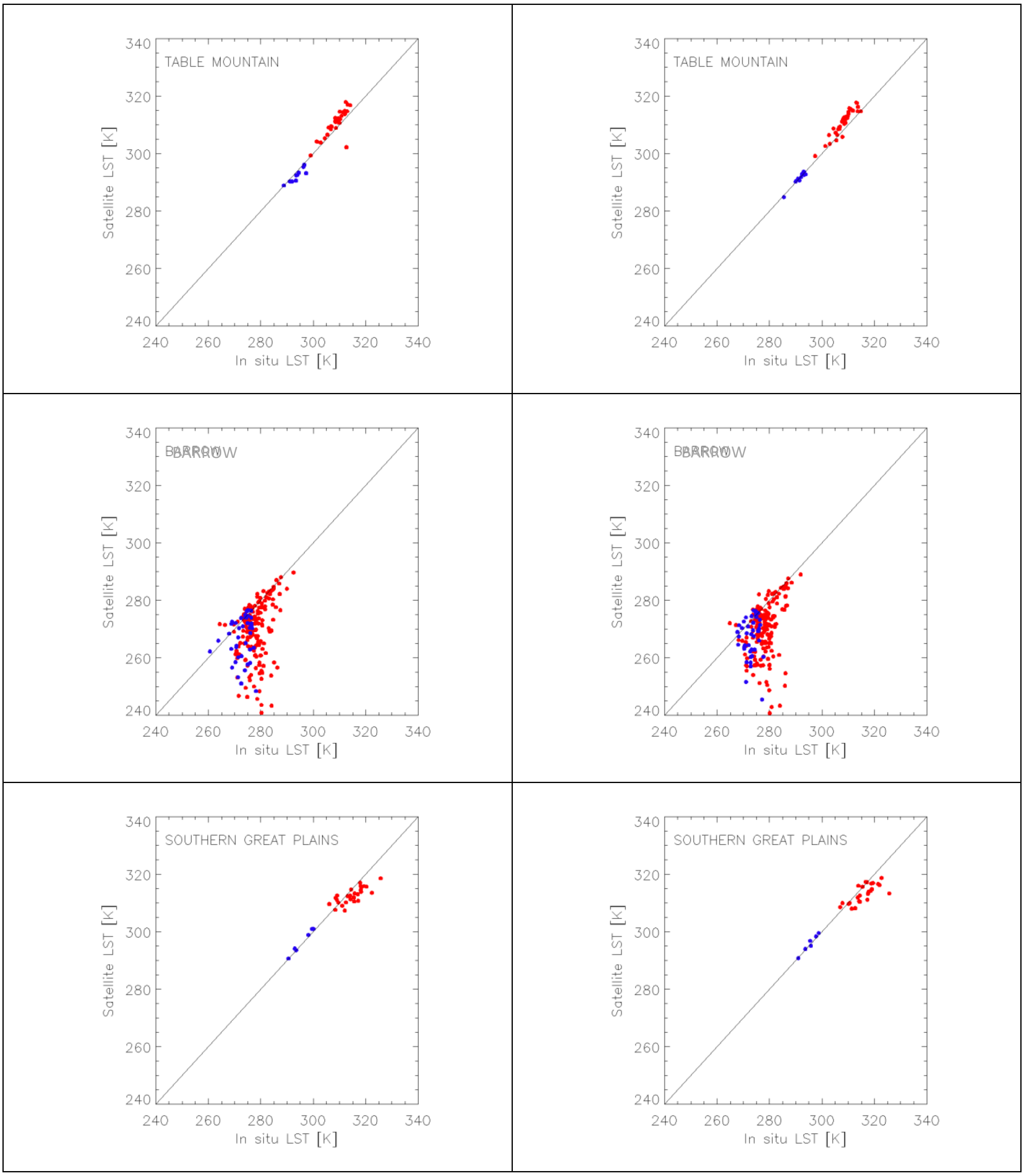
TABLE MOUNTAIN
TABLE MOUNTAIN
BARROW
BARROW
SOUTHERN GREAT PLAINS
SOUTHERN GREAT PLAINS
Satellite LST [K]
In situ LST [K]
240
260
280
300
320
340

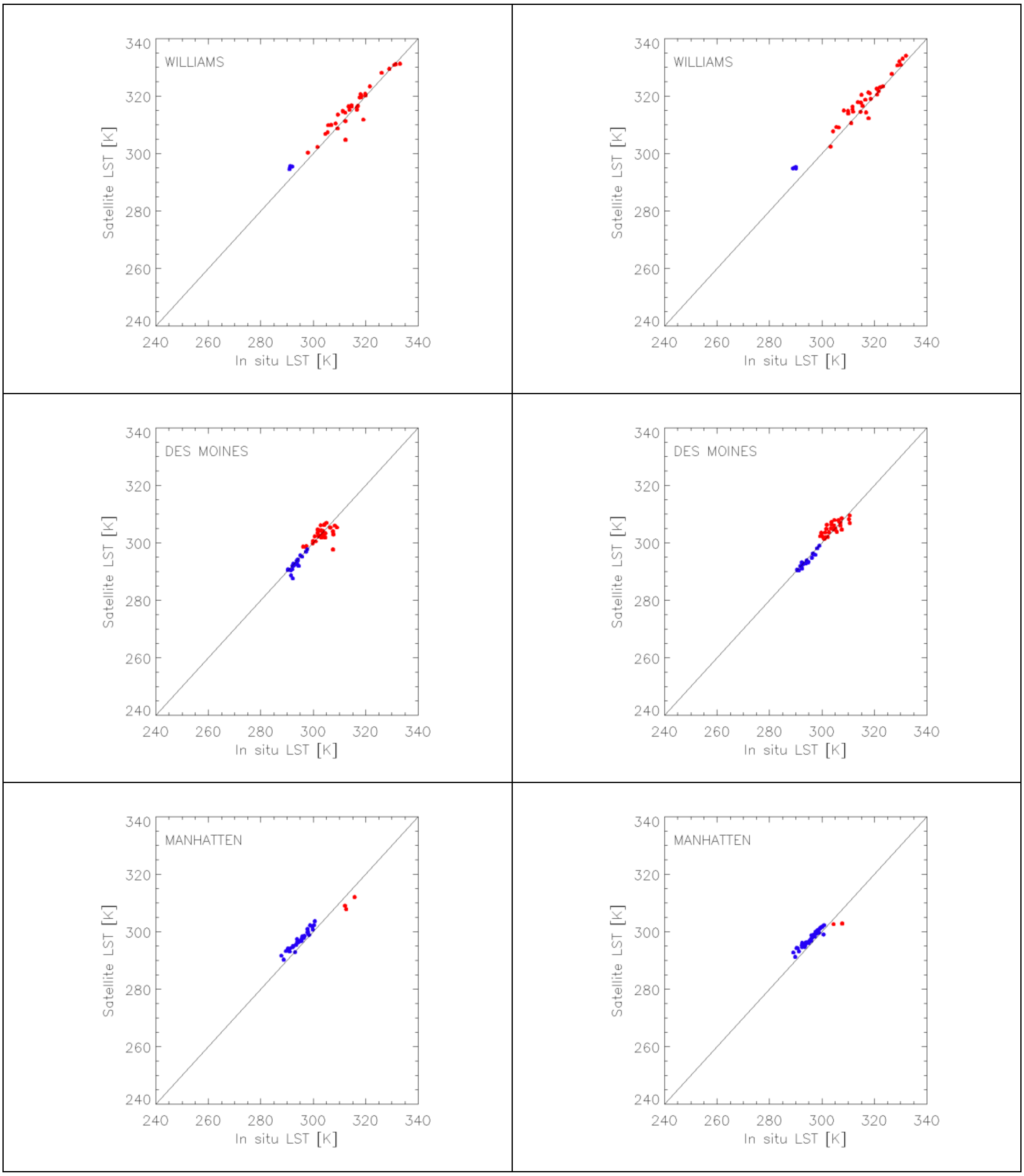

*Figure 28: Validation of the SL_2_LST product in Q3 2023 for SLSTR-A (left) and SLSTR-B (right) at twelve Gold Standard in situ stations of the SURFRAD network plus two Gold Standard station from the ARM network. The matchups are split between daytime (red) and night-time (blue).*

As with past cycles cloud has reduced the number of matchups per station to single figures for most stations during day or night, with some missing statistics entirely. It is therefore challenging to determine robust statistics. The cumulative statistics are presented in each Annual Report. Nonetheless, it can be seen that overall the matchups are in general close to the 1:1 line with few outliers. There is a small systematic bias evident at some stations, particularly during the day, which may indicate an update to the retrieval coefficients may be worth exploring. Some cloud over-masking (night-time) and under-masking (daytime) appears for some of the sites, and may be worth exploring whether the cloud coefficients need further fine tuning. This is certainly the case for the Barrow site.

## 6.2 Category-C validation

This section will be updated shortly.

## 6.3 Level-3C Assessment

This section will be updated shortly.

## 6.4 References

Augustine, J.A. and Dutton, E.G. (2013). Variability of the surface radiation budget over the United States from 1996 through 2011 from high-quality measurements. Journal of Geophysical Research: Atmospheres 118, 43–53.

Ghent, D. J., Corlett, G. K., Göttsche, F.-M., & Remedios, J. J. (2017). Global land surface temperature from the Along-Track Scanning Radiometers. Journal of Geophysical Research: Atmospheres, 122. https://doi.org/10.1002/2017JD027161

Guillevic, P., Göttsche, F., Nickeson, J., Hulley, G., Ghent, D., Yu, Y., Trigo, I., Hook, S., Sobrino, J.A., Remedios, J., Román, M. & Camacho, F. (2017). Land Surface Temperature Product Validation Best Practice Protocol. Version 1.0. In P. Guillevic, F. Göttsche, J. Nickeson & M. Román (Eds.), Best Practice for Satellite-Derived Land Product Validation (p. 60): Land Product Validation Subgroup (WGCV/CEOS), doi:10.5067/doc/ceoswgcv/lpv/lst.001

Morris, V.R. Infrared Thermometer (IRT) Handbook (ARM TR-015) (2006). Technical report, Atmospheric Radiation Measurement, Climate Research Facility, U. S. Department of Energy.

Schneider, P., Ghent, D., Corlett, G., Prata, F., and Remedies, J. (2012). AATSR validation: LST validation protocol. Internal publication, UL-NILU-ESA-LST-LVP Issue 1 Revision 0, page 1-39. http://lst.nilu.no/Portals/73/Docs/Reports/UL-NILU-ESA-LST-LVP-Issue1-Rev0-1604212.pdf.

Stoffel, T. Ground Radiation (GNDRAD) Handbook (ARM TR-027) (2006). Technical report, Atmospheric Radiation Measurement, Climate Research Facility, U. S. Department of Energy.

Trigo, I. F., Monteiro, I. T., Olesen, F., & Kabsch, E. (2008). An assessment of remotely sensed land surface temperature. Journal of Geophysical Research, 113(D17), D17108. https://doi.org/10.1029/2008JD010035

# 7 Level 2 FRP validation

## 7.1 The SLSTR Fire Radiative Power product

The SLSTR FRP NTC product (both SLSTR-A and SLSTR-B) has been released to the public on August 19th, 2020. The current processing baseline for SLSTR-A and SLSTR-B FRP products is FRP_NTC.004.07.00 and was deployed in the Land processing centres on February 28th, 2022, for both SLSTR-A and for SLSTR-B. This baseline is including an updated FRP algorithm, called FRP V2. This updated algorithm is based on the previous one, with a similar nighttime algorithm, but includes improved thermal fire detection over daytime products. Daytime detection is performed using a mixed thermal band. The S7 brightness temperature is considered by default for all pixels. In the event of saturation, the F1 channel is used instead for the saturated pixel, and all pixels around it in a 11 x 11 pixels window that either have a S7 brightness temperature above 300 K, or a brightness temperature difference between S7 and S8 higher than 10 K. AF detection during nighttime remains similar to that of the FRP V1 algorithm and uses the F1 measurements. The FRP V2 algorithm also introduced an alternative fire detection using SWIR channels, however this functionality is not yet part of the validation report.

This report only focuses on measurements obtained from the thermal channels using the FRP V2 algorithm over the months of April, May, and June. First, the fires detected during nighttime are assessed. Then, the same analysis is repeated for daytime fires.

## 7.2 Validation methodology

Validation of the SLSTR L2 FRP products can be performed using either in-situ data such as airborne measurements or using products from a reference satellite for inter-comparison. Active fires in situ data are unfortunately not frequent enough to validate fire satellite data products on an operational basis. The current comparison methodology uses products from NASA Moderate-Resolution Imaging Spectroradiometer (MODIS) as reference fire data for the intercomparisons.

This present inter-comparison, initially based on previous work from M. Wooster and W. Xu on the FRP Prototype and on the evaluation of SEVIRI fire data, aims to assess two things:

(i) The detection of fires' position and extent in time and space.

(ii) The estimated radiative fire power (FRP) of active fires.

To do so, the SL_2_FRP product from SLSTR-A and SLSTR-B are compared with the operational MODIS MOD14 FRP product from MODIS Terra. This inter-comparison should not be interpreted as a full validation exercise but rather as a check of the consistency of the FRP products derived from the satellites, as ground truth is not available.

The methodology to obtain data fit for comparison purposes is outlined hereafter:

- Once areas of interest have been defined, identify all SL_2_FRP scenes containing active fires;
- Download MODIS MOD14 data with a scene overpass time within ± 6 minutes from that of SLSTR;
- Restrict observations to a scan angle of ±20° or equivalent pixel area of 1.7 km$^2$ to avoid edge-of-swath data, and to the common area of detection between the two products. The scan angle was decreased from ±30° to limit possible pixel size discrepancies between MODIS and SLSTR data;

- Reproject MODIS pixels on the SLSTR F1 grid. If multiple MODIS active fire pixels (AFP) are present in the same equivalent SLSTR grid cell, their combined FRP is used.

Omissions, commissions, and double detections are then evaluated. A fire is classified as omitted if no SLSTR fire pixel is present in a 7 x 7 pixels window around a MODIS fire pixel. Conversely, a fire is classified as commissioned if no MODIS fire pixel is present in a 7 x 7 pixels window around a SLSTR fire pixel. If SLSTR and MODIS pixels are present within the windows, the fire is classified as double detected.

The FRP analysis is twofold: it is done both at the pixel level, and at the cluster level. A cluster is defined as fires close enough to be interpreted as a single fire event (i.e. the detected fire pixels are next to one another). In both cases, as MODIS FRP data is provided before atmospheric correction, they are atmospherically corrected using the water vapor content estimated by Sentinel 3 as the basis to compute the transmission.

The detected fire clustering is done according to the following procedure: for both sensors, a connected-component labeling using an 8-connectivity is used to label clusters. Then, iteratively, clusters from one satellite having an overlap with clusters from the other are merged to form superclusters, until each supercluster from one satellite only overlaps with a single supercluster from the other. Figure 29 illustrates the process. Finally, superclusters associated with problematic flags (clouds/water/detection/high S7-S8 difference) are removed from the datasets. The remaining matching pairs of SLSTR and MODIS superclusters are used for further analysis regarding FRP estimates.

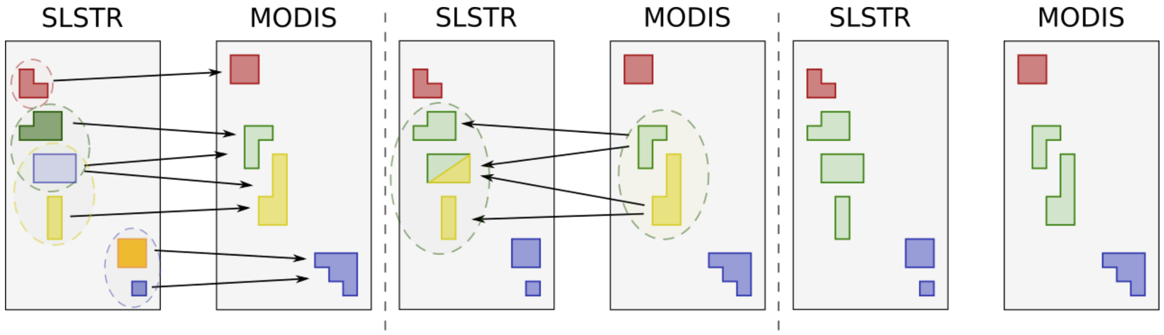

***Figure 29: Formation process of the pairs of superclusters depending on AFP detected each satellite. Fire clusters and superclusters are identified by their colors. At the end of the process, pairs of SLSTR and MODIS superclusters share the same color.***

Four areas of high fire activity between July 1st and September 30th were selected: western Canada, Europe, Central Africa, and China (see Figure 30). Since the last report, a mean of assessing the FRP estimated from the SWIR bands through cross-comparison with those of the MWIR bands was included.

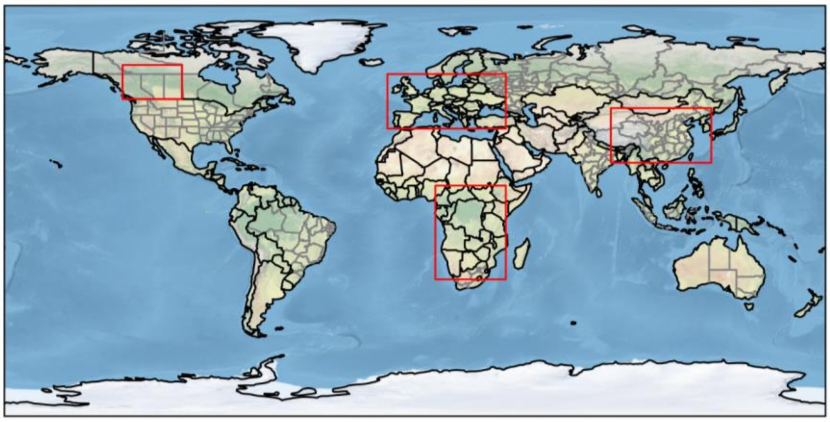

*Figure 30: Selected zones for the intercomparison over the July-September 2023 period*

## 7.3 Results

### 7.3.1 Global distributions of the fires

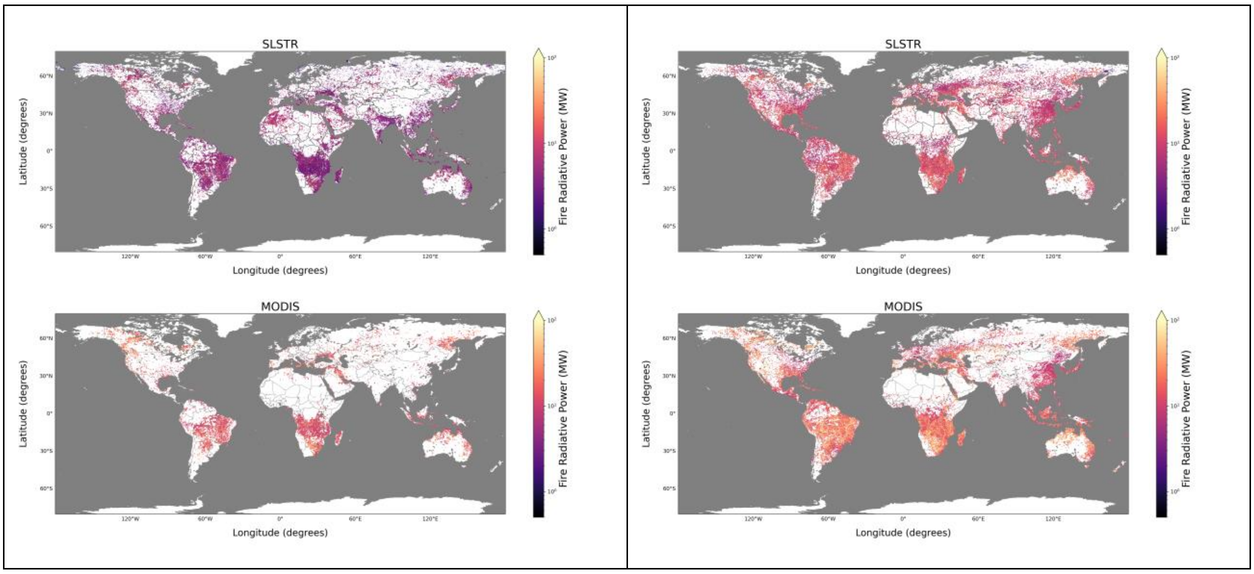

*Figure 31: Fires detected by SLSTR and MODIS at nightime (left) and daytime (right).*

Figure 31 shows the location and radiative power of fires detected by SLSTR and MODIS during night and daytime. On one hand, SLSTR seems to be detecting more fire than MODIS during nighttime, most of them having a lower intensity, while there are few omissions. On the other hand, during daytime, omissions seem to be much more frequent, especially in the southern hemisphere, with large swathes of Brazil, southern Africa, and Australia presenting MODIS fires when no fire was detected by SLSTR.

## 7.3.2 Nighttime Fires Validation

### 7.3.2.1 MWIR fires

Table 9 presents a summary of the intercomparison between active fires detected by SLSTR and MODIS over the July—September 2023 period, as well as past periods. As for previous periods, the data present a significantly larger quantity of commissions (about half of SLSTR-detected fires are commissions) compared to the omissions. Omissions are stable compared to the previous period, during which refinements in the reprojection between MODIS and SLSTR grids were introduced. The FRP distributions of both MODIS and SLSTR clusters are both higher than past periods before April 2023 for the 25th, 50th, and 75th percentile values. While this may be due to the occurrence of more intense fires, it may also be due to the updated clustering values introduced since April.

***Table 9: Summary of the intercomparison between nighttime SLSTR and MODIS active fires over the July—September 2023 period. Results from previous 3-months comparisons are included for information purposes.***

| **Variable** | **Value** | | | | |
|---|---|---|---|---|---|
| | **2023** | | | **2022** | |
| | **Jul.—Sep.** | **Apr.—Jun.** | **Jan.—Mar.** | **Oct.—Dec.** | **Jul.—Sep.** |
| Commissions (% of total SLSTR AFP) | 54% | 49% | 56% | 55% | 62% |
| Omissions (% of total MODIS AFP) | 3% | 3% | 14% | 17% | 18% |
| SLSTR AFP double detec. (% of total SLSTR AFP) | 46% | 51% | 44% | 45% | 38% |
| MODIS AFP double detec. (% of total MODIS AFP) | 97% | 97% | 86.0% | 83% | 82% |
| Total SLSTR AFP | 82,970 | 19,265 | 26,911 | 23,758 | 32,239 |
| Total MODIS AFP | 10,921 | 3,323 | 4,048 | 4,035 | 4,972 |
| Percentiles 25, 50, 75 of SLSTR clusters FRP (MW) | 19, 39, 102 | 10, 34, 61 | 11, 19, 35 | 12, 21, 40 | 12, 22, 43 |
| Percentiles 25, 50, 75 of MODIS clusters FRP (MW) | 10, 25, 72 | 17, 23, 79 | 7, 12, 23 | 8, 14, 30 | 8, 14, 31 |
| Mean bias of FRP per cluster (MW) | 17 | -59 | 7 | 7 | 5 |
| Median of FRP scatter per cluster (MW) | 9 | 8 | 5 | 6 | 5 |

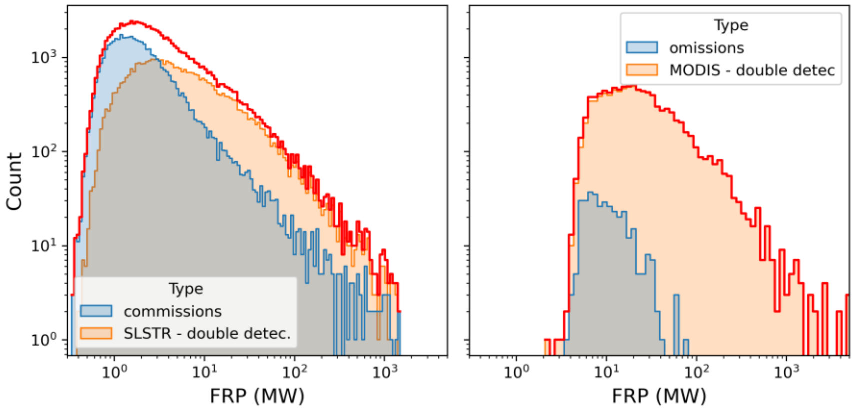

***Figure 32: For nighttime: (left) in red, the histogram of all FRP estimated from SLSTR; in blue and orange, a breakdown between commissions and double detections, respectively. (right) in red, the histogram of all FRP estimated from MODIS; in blue and orange, a breakdown between commissions and double detections, respectively.***

As visible in Figure 32, a large proportion of the fire pixels SLSTR detects present a very low FRP (< 4 MW). Conversely, almost fire pixel detected by MODIS had a FRP above 4 MW. The distribution of the FRP of commission pixels confirms that almost all commissions concern fires with very low FRP, highlighting the fact that SLSTR is much more sensitive than MODIS to detect active fires. Omissions, on the other hand, concern fires of very common intensities (~10 MW). Figure 33 shows that there is a good agreement between the FRP of clusters detected by MODIS and those detected by SLSTR. For low FRP values, SLSTR clusters seem to be more intense, which is in line with the lower threshold of SLSTR to detect an AFP: this allows for the detection of larger low-intensity clusters. Overall, the median absolute error between MODIS and SLSTR cluster FRP is 15 MW.

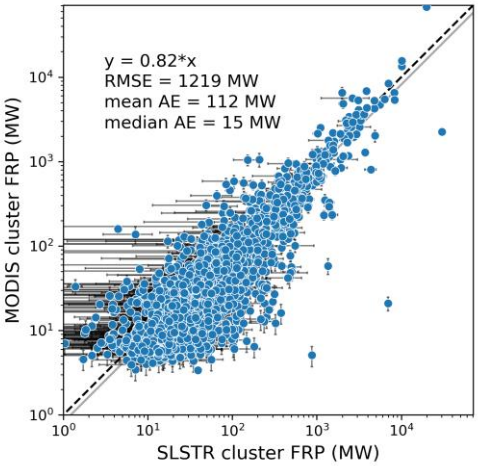

*Figure 33: Comparison between the FRP of cluster pairs detected by SLSTR and MODIS during nighttime*

#### 7.3.2.2 SWIR fires

The AFP and FRP detected by the SWIR channels are now part of this validation report. Only the FRP value estimated from the SWIR channels is validated, through by cross-comparison with those estimated from the MWIR channels. As SWIR and MWIR channels do not have the same sampling grid (500 m vs 1 km), the validation algorithm is as follow:

1. Reproject the SWIR fires on the MWIR grid using nearest-neighbours;
2. Cluster the SWIR fires and link them to MWIR fires (as done in Figure 29 with SLSTR MWIR and MODIS);
3. Compute the total FRP value of SWIR and MWIR cluster. For MWIR clusters, only take into account the FRP of pixels for which there is an associated SWIR value;
4. Compare estimated MWIR and SWIR cluster FRP.

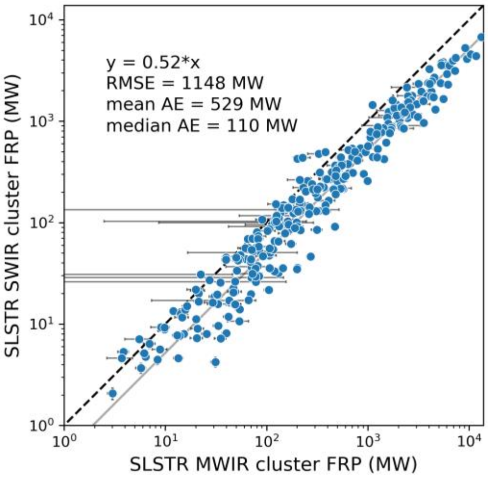

***Figure 34: Comparison between the FRP of cluster pairs detected by SLSTR MWIR and SWIR bands during nighttime.***

Figure 34 shows that there is a good correlation between the FRP of clusters detected by the MWIR and the SWIR bands over the whole range. However, it appears that there is a difference in the intensity of the cluster FRP estimated by the bands: SWIR cluster FRP is, overall, half the intensity of the MWIR cluster FRP (slope of 0.52). Since for this comparison the extents of MWIR clusters were limited to those of SWIR cluster, it appears that the SWIR bands lead to lower FRP for the same fire events.

### 7.3.3 Daytime Fires Validation

Table 10 presents a summary of the intercomparison between active fires detected by SLSTR and MODIS over the July—September 2023 period, as well as past periods. The proportion of commissioned fire pixel is in line with previous periods, while the proportion of omissions is in line with the April—June 2023 period. This difference in proportion between before and after April 2023 corresponds to the introduction of the improvements in the MODIS-SLSTR grid matching improvements. The FRP distributions of both MODIS and SLSTR clusters are higher than past periods before April 2023 for the 25th, 50th, and 75th percentile values. While this may be due to the occurrence of more intense fires, it may once again be due to the updated clustering values introduced since April.

*Table 10: Summary of the intercomparison between daytime SLSTR and MODIS active fires over the July-September 2023 period. Results from previous 3-months comparisons are included for information purposes.*

| Variable | Value | | | | |
|---|---|---|---|---|---|
| | 2023 | | | 2022 | |
| | Jul.—Sep. | Apr.—Jun. | Jan.—Mar. | Oct.—Dec. | Jul.—Sep. |
| Commissions (% of total SLSTR AFP) | 43% | 31% | 27% | 48% | 49% |
| Omissions (% of total MODIS AFP) | 33% | 27% | 42% | 46% | 49% |
| SLSTR AFP double detec. (% of total SLSTR AFP) | 57% | 69% | 73% | 52% | 51% |
| MODIS AFP double detec. (% of total MODIS AFP) | 67% | 73% | 58% | 54% | 51% |
| Total SLSTR AFP | 37,754 | 22,069 | 16,257 | 11,163 | 15,667 |
| Total MODIS AFP | 20,458 | 10,930 | 14,946 | 8,114 | 11,565 |
| Percentiles 25, 50, 75 of SLSTR clusters FRP (MW) | 18, 36, 86 | 17, 37, 90 | 15, 28, 51 | 17, 27, 52 | 16, 27, 54 |
| Percentiles 25, 50, 75 of MODIS clusters FRP (MW) | 15, 32, 82 | 19, 35, 91 | 12, 22, 46 | 13, 22, 43 | 14, 23, 50 |
| Mean bias of FRP per cluster (MW) | -9 | -13 | 6 | 4 | 5 |
| Median of FRP scatter per cluster (MW) | 3 | 3 | 4 | 4 | 3 |

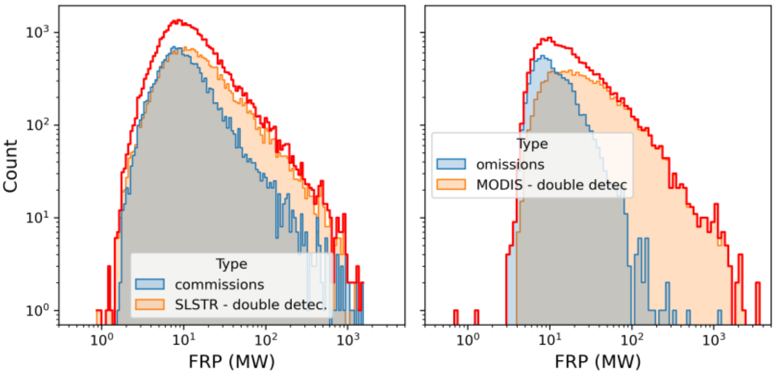

***Figure 35: From left to right, for daytime: histograms of the FRP of fires detected by SLSTR and MODIS, histogram of the FRP of commissions, histogram of the FRP of omissions.***

Figure 35 is the equivalent to Figure 32, but for daytime. The same patterns are observed: a large proportion of the fire pixels SLSTR detects present a very low FRP (< 4 MW), unlike MODIS. In a similar fashion as for nighttime, commissions almost exclusively present very low FRP values, while omissions are, for the most part, average-intensity fires.

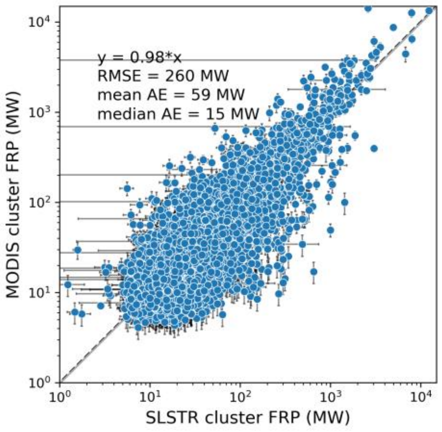

***Figure 36: Comparison between the FRP of cluster pairs detected by SLSTR and MODIS during daytime.***

### 7.3.4 Biome influence on active fire detection

The present section consists in a preliminary study on the biome influence over errors of commission and omission. The biome corresponding to each fire is determined using the Global Land Cover 2000 data. This per-biome analysis may help identify biome-dependent behaviours concerning active fire detection. For each biome, over nighttime and daytime, the absolute numbers of commissions and omissions as well as the relative numbers (with regards to the total number of SLSTR and MODIS AFP for commissions and omissions, respectively) are evaluated over the July—September 2023 period.

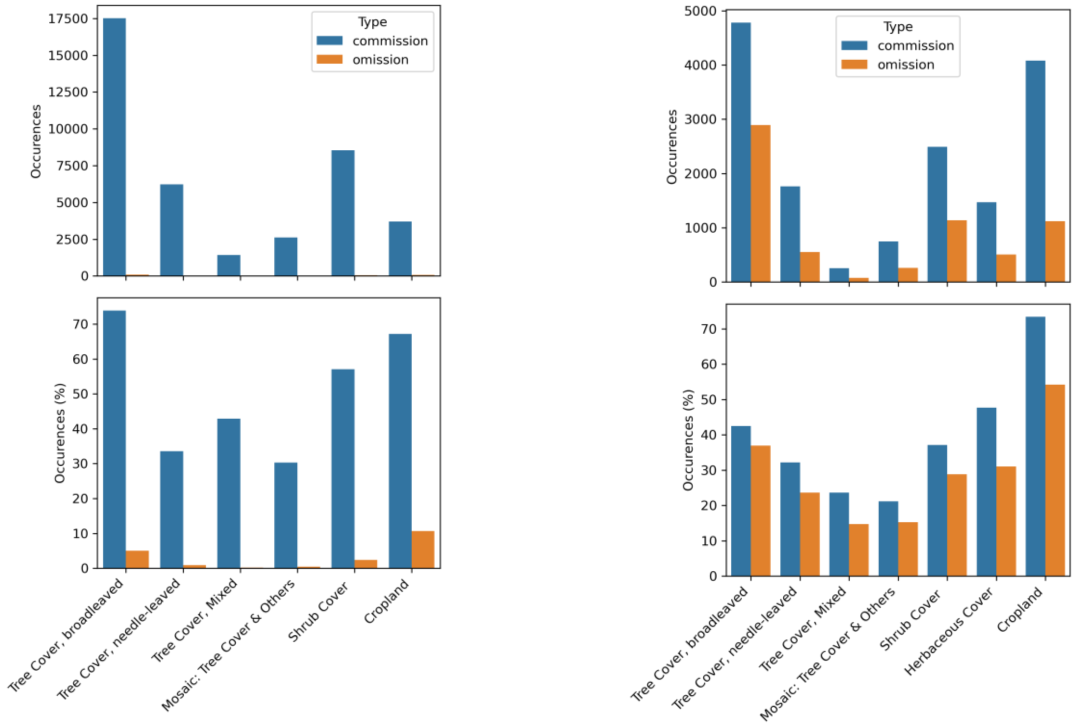

*Figure 37: Occurrences of commissions and omissions of active fire pixels per biome. On the left, nighttime; on the right, daytime.*

Figure 37 shows the absolute (top) and relative number (bottom) of commissions and omissions. For clarity purposes, similar biomes were aggregated together, while some were rejected from the analysis. For both nighttime and daytime, the percentage of commissions from Treed Needle-leaved Evergreen is lower than the average, with values around 30% in both cases, versus 54% and 43% commissions on average for nighttime and daytime, respectively. As with the previous period, the Treed Broadleaved biomes have higher than average percentages of commissions (more than 70% for nighttime) with non-negligible quantities of active fire detections. For daytime, croplands also present a very high number of commissions, which might correspond to low intensity agricultural burnings.

## 7.4 Conclusion

This performance report seems to confirm that the accuracy improvements of the geographic locations of fires in the FRP monitoring algorithm put in place for the last report have led to a reduction in the number of commissions and omissions compared to previous periods.  This period, as the last one, showed that the active fires detected by the satellites were much more in line, with increased numbers of double detections.

Overall, in line with previous reports, it appears that for both nighttime and daytime products, much more AFP are detected by SLSTR than MODIS. Indeed, SLSTR's FRP threshold to detect active fires is much lower than that of MODIS (<1 MW vs ~3 MW), leading to a very high number of low intensity commissioned fires.

For most active fire clusters, trends are coherent with past periods, with good agreement between SLSTR and MODIS clusters' FRP. The reduction in maximum scan angle from 30° to 20° may have contributed to the better relationship between SLSTR and MODIS cluster, as possible pixel size discrepancy was more limited. Overall, for both daytime and nighttime, there seem to be a linear relationship between MODIS and SLSTR cluster FRP, and a median absolute error of 15 MW.

The analysis of the FRP estimated from the SWIR bands showed that while there is indeed a linear relationship between the SWIR cluster and their SWIR counterparts, the relation is not 1:1. Presently, it appears that cluster FRP estimated from the SWIR bands is about half of that estimated from the MWIR bands (factor of 0.52). Further analysis of the SWIR FRP values and distribution, as well as fire location, is needed.

The results of the per-biome analysis seem to confirm behavioural differences between Broadleaved and Needle-leaved biomes: although both present high quantities of fire detections, as would be expected from forests, the former are much more prone to commissions than the latter (>70% versus ~30% and ~40% versus ~30%, for nighttime and daytime, respectively). Shrublands and Croplands presented a very high quantity of commissions at nighttime, and Croplands still presented a very high number of commissions during daytime (>70%). This may be explained by the lower detection threshold of SLSTR (~1 MW), which may detect smaller agricultural fires

# 8 Appendix A

All Data Quality Reports, as well as past years Data Quality Reports and Annual Performance Reports, are available on dedicated pages in Sentinel Online website, at:

- https://sentinel.esa.int/web/sentinel/technical-guides/sentinel-2-msi/data-quality-reports
- https://sentinel.esa.int/web/sentinel/technical-guides/sentinel-3-olci/data-quality-reports
- https://sentinel.esa.int/web/sentinel/technical-guides/sentinel-3-slstr/data-quality-reports
- OPT Annual Performance Report Year 2022 (PDF document)

***End of document***